TAMPEREEN TEKNILLINEN YLIOPISTO
TAMPERE UNIVERSITY OF TECHNOLOGY

Aino Leppänen

Modeling Fume Particle Dynamics and Deposition with Alkali Metal Chemistry in Kraft Recovery Boilers

Julkaisu 1273 • Publication 1273

Tampere 2015

Tampereen teknillinen yliopisto. Julkaisu 1273
Tampere University of Technology. Publication 1273

Aino Leppänen

Modeling Fume Particle Dynamics and Deposition with Alkali Metal Chemistry in Kraft Recovery Boilers

Thesis for the degree of Doctor of Science in Technology to be presented with due permission for public examination and criticism in Festia Building, Auditorium Pieni Sali 1, at Tampere University of Technology, on the 9th of January 2015, at 12 noon.

Tampereen teknillinen yliopisto - Tampere University of Technology
Tampere 2015

Doctoral candidate: Aino Leppänen
Department of Chemistry and Bioengineering
Tampere University of Technology, Tampere, Finland

Supervisor: Professor Antti Oksanen
Department of Chemistry and Bioengineering
Tampere University of Technology, Tampere, Finland

Pre-examiners: Professor Larry L. Baxter
Department of Chemical Engineering
Brigham Young University, Provo, Utah, USA

Adjunct Professor Andrew Jones
Chemical Engineering & Applied Chemistry
University of Toronto, Toronto, Ontario, Canada
and International Paper, Loveland, Ohio, USA

Opponent: Professor Dr. Ing. Roman Weber
Institute for Energy Process Engineering and Fuel Technology
Clausthal University of Technology, Clausthal-Zellerfeld, Germany

ISBN 978-952-15-3433-1 (printed)
ISBN 978-952-15-3436-2 (PDF)
ISSN 1459-2045

ABSTRACT

The kraft recovery boiler is the largest single unit in the pulp-making process, which makes its reliable operation important. However, the fuel of the recovery boiler, black liquor, contains large quantities of ash-forming elements that pose challenges to the efficient operation of the boiler. A fraction of these elements vaporizes in the recovery boiler and condenses to form submicron-sized particles, called fume. The fume particles may form fouling deposits on the heat transfer surfaces, cause plugging of the flue gas channels, and even expose the surfaces to corrosion. These problems often lead to unscheduled shutdowns of the boiler, which are expensive due to the large size of the modern pulp mills. Significant savings could be achieved if the behavior of the ash-forming elements could be better predicted.

The objective of this thesis is to develop a CFD-based (computational fluid dynamics) model for the alkali metal chemistry, fume particles, and fume deposits in the kraft recovery boiler, and to use the model to simulate real recovery boilers. The model combines 3-dimensional CFD, fine particle dynamics, and equilibrium chemistry in a novel way, and solves the fume particle and deposit composition at different locations in the superheater area of the boiler. The model contains certain limitations, such as the steady-state approximation because a compromise has to be made between accuracy and computational cost, which is a significant factor when developing tools for industrial use.

The model has been partially validated with measurements in an operating recovery boiler, and the modeling results are in good qualitative agreement with the measurements. Furthermore, the modeling results suggest that deposition through thermophoresis is the main mechanism of fume deposit formation in a recovery boiler, but also that the direct condensation of alkali chloride vapors to heat transfer surfaces can be significant if the black liquor chlorine content is high. According to the model sensitivity analysis, fume deposit growth seems to be a self-limiting process, since an increase in the deposit thickness lowers the rate of deposition by thermophoresis. Another important result is that chlorine enriches in the deposit layers closer to the tube surfaces, which is a result of the high temperature dependence of alkali chloride condensation.

The CFD-based model developed here improves understanding of the fume formation mechanisms, shedding light on processes that would be difficult to investigate through experimental methods alone in the corrosive boiler environment. In particular, the model can simulate how certain operational changes, such as increasing boiler load or steam temperatures, affect the alkali metal and fume behavior. In the future, the model can be utilized in the industry to support the engineering of new recovery boilers, and minimize fouling, plugging, and corrosion problems.

PREFACE

This work was carried out in Tampere University of Technology in the Department of Energy and Process Engineering (2011–2012) and the Department of Chemistry and Bioengineering (2013–2014). The financial support received from Valmet Power (former Metso Power), Tampere University of Technology, the Finnish Graduate School in Computational Fluid Dynamics of the Academy of Finland, Walter Ahlström foundation, KAUTE (Finnish Science Foundation for Economics and Technology), the Finnish Foundation for Technology Promotion (Tekniikan edistämissäätiö), and A. R. Winter foundation is gratefully acknowledged.

I would like to thank my supervisor, Prof. Antti Oksanen, for offering me this interesting thesis topic, for guidance, and for ensuring that I could focus on the thesis. I am also grateful to Erkki Välimäki from Valmet Power for investing his time in my thesis and for introducing me to the world of recovery boilers. The help of many others in Valmet has also been invaluable: Anne Aikio, Dr. Sonja Enestam, Kari Haaga, Ville-Pekka Heikkilä, Hanna Kinnunen, Jarmo Mansikkasalo, Jukka Mäkinen, and Piia Niemi, thank you for contributing to my work. I would also like to thank my closest colleagues, Anna, Tiina, Henrik, Georgios, Matti, and Fanni for sharing the ups and downs of research work.

I deeply appreciate the guidance of Prof. Honghi Tran during my visit in the Pulp and Paper Centre of the University of Toronto. The visit and our continued co-operation have been crucial to the progress of my research. I would also like to thank my other colleagues and friends in Toronto for making me feel so welcomed there. I would like to acknowledge Dr. Jouni Pyykönen from VTT for his preliminary work on fine particle modeling in the recovery boiler and for helping me at the beginning of my work. I have also received valuable advice from Dr. Markus Engblom and Dr. Daniel Lindberg from Åbo Akademi University, Prof. Esa Vakkilainen from Lappeenranta University of Technology, and Dr. Evan Whitby concerning the FPM program. I would also like to thank the Tampere Center for Scientific Computing for patiently helping me, and Alan Thompson for proofreading this thesis.

Finally, I would like to thank those who have not been directly involved with my thesis, but have nevertheless helped me write it. Teekkarikuoro and my friends outside the university, thank you for reminding me that it is not all about research. The Student Union of TUT and the Guild of Environmental and Energy Technology, thank you for providing me a sense of belonging already at the beginning of my university studies. My heartfelt thanks to my cousin Sofia and my friend Jatta for encouraging me. My parents and my sister Maija, thank you for always believing in me, even if I myself could not. Lastly, thank you Toni for carrying at least half of the weight of this thesis. I simply would not be here without you.

Tampere, December 3, 2014

Aino Leppänen

LIST OF PUBLICATIONS

This thesis is based on the following four publications, referred as Publications I–IV. Additionally, some unpublished material is presented and discussed.

I Leppänen, A., Välimäki, E. and Oksanen, A. Modeling fine particles and alkali metal compound behavior in a kraft recovery boiler. *TAPPI Journal*, 11(7): 9–14, 2012.

II Leppänen, A., Välimäki, E., Oksanen, A., and Tran, H. CFD-modeling of fume formation in kraft recovery boilers. *TAPPI Journal*, 12(3):25–32, 2013.

III Leppänen, A., Tran, H., Taipale, R., Välimäki, E., and Oksanen, A. Numerical modeling of fine particle and deposit formation in a recovery boiler. *Fuel*, 129:45–53, 2014.

IV Leppänen, A., Tran, H., Välimäki, E., and Oksanen, A. Modelling fume deposit growth in recovery boilers: effect of flue gas and deposit temperature. *J-FOR: Journal of Science & Technology for Forest Products and Processes*, 4(1):50–57, 2014.

AUTHOR'S CONTRIBUTION

I The author developed further the original idea of Dr. J. Pyykönen and implemented the alkali metal and fine particle model in a recovery boiler furnace. The author carried out the simulations and wrote the manuscript.

II The author improved the model presented in Paper I and implemented it to the recovery boiler superheater area. The author carried out the simulations, compared the results with the literature values, and wrote the manuscript.

III The author extended the model presented in the previous papers by implementing fume deposit formation. The author carried out the simulations in a new recovery boiler, and compared the modeling results with the measurement results obtained in this boiler. The author took part in the measurement campaign. The author wrote the manuscript.

IV The author planned and carried out the simulations for a model sensitivity analysis and wrote the manuscript.

LIST OF SYMBOLS AND ABBREVIATIONS

Latin symbols

A	constant	-
C	constant	-
C	Cunningham slip correction factor	-
C	heat capacity	J/K
$\mathbf{c}$	drift velocity vector	m/s
D	diffusion coefficient	m^2/s
d	diameter	m
EF	enrichment factor	-
G	Gibbs energy	J
H	enthalpy	J
h	specific enthalpy	J/kg
I	mass flux	$kg/(m^2 \cdot s)$
i	mole fraction of K or Cl	
K	multiplier for thermophoresis	-
k	thermal conductivity	$W/(m \cdot K)$
k	turbulent kinetic energy	J/kg
Kn	Knudsen number	-
M	moment	(various)
m	mass	kg
N	total number concentration	$1/m^3$
n	number concentration	$1/m^3$
p	pressure	Pa
R	gas constant	$J/(K \cdot mol)$
Re	Reynolds number	-
S	entropy	J/K
S	saturation ratio	-
S	source term	(various)
Sc	Schmidt number	-
Sh	Sherwood number	-
T	temperature	K
t	time	s
u	velocity	m/s
v	velocity	m/s
$\mathbf{v}$	velocity vector	m/s
x	spatial coordinate	m

Greek symbols

α	accommodation coefficient	-
ε	turbulent dissipation rate	J/(kg·s)
λ	mean free path	m
μ	dynamic viscosity	kg/(m·s)
ν	kinematic viscosity	m^2/s
ρ	density	kg/m^3
σ	standard deviation	-
ϕ	conserved intensive property	(various)

Subscripts

ave	average
BL	black liquor
c	characteristic
$coag$	coagulation
$diff$	diffusion
ds	dry solids
fume	fume particle or deposit
g	gas
g	geometric
$growth$	particle growth
H	hydraulic
i	index
i	potassium or chlorine
j	index
k	index
l	number of molecules in a particle
m	name of a constant
n	mean
p	constant pressure
p	particle
S	saturation
s	name of a constant
T	thermophoresis by Talbot
t	name of a constant
th	thermophoresis
u	universal
v	vapor

w	wall
WS	thermophoresis by Waldmann and Schmidt
ϕ	conserved intensive property

Abbreviations

ABC	Aerosol Behavior in Combustion [1, 2]
bb	boiler bank
CFD	computational fluid dynamics
D	dimensional
DPM	Discrete Phase model [3]
ESP	electrostatic precipitator
FPM	Fine Particle Model [4]
GDE	general dynamic equation
ISP	intermediate size particle
MAD	modal aerosol dynamics
RANS	Reynolds-averaged Navier-Stokes
SEM	scanning electron microscope
sh	superheater
UDF	user-defined function
wt	weight

Contents

Chapter 1

Introduction

The kraft recovery boiler treats the waste stream of the pulp-making process, black liquor, and is the largest unit in the process. The recovery boiler has a dual function: the recovery of the used pulping chemicals and the production of energy for further use in the pulp mill and the possible adjacent paper mill. In addition, modern recovery boilers often produce excess electricity for the power grid, which makes them important producers of bioenergy. However, the electricity produced in the recovery boiler is limited by the high amount of ash-forming elements (Na, K, S, and Cl) in black liquor, which can cause corrosion of the heat transfer tubes. Nowadays, the highest steam temperatures in a recovery boiler are 515 °C [5], which are significantly below the power boiler steam temperatures, which can exceed 600 °C [6].

The ash-forming elements in black liquor are partly vaporized in the boiler furnace to form gaseous sodium (Na) and potassium (K) salts, which, upon flue gas cooling, condense into submicron-sized fine particles, called fume. These salts can also form deposits on the heat transfer surfaces as illustrated in Fig. 1.1, showing boiler bank tubes with a snow-like fume deposit on them. The fume deposits can lower the heat transfer rate in the superheater tubes, plug the flue gas flow, and expose the heat transfer surfaces to corrosion, especially if the salts contain chlorine (Cl). Problems in the heat transfer surfaces may then force an unscheduled shutdown of the boiler, which is very expensive. In order to overcome these problems and still increase the electricity production, more information is needed on the behavior of the ash-forming elements in the recovery boiler. However, conducting measurements is difficult in the hot and corrosive boiler environment.

In the 1990s, Jokiniemi et al. [1, 2] developed a computer model that simulated the behavior of the ash-forming elements and fume in the kraft recovery boiler with the help of fine particle dynamics and equilibrium chemistry. However, the model was only 1-D (one-dimensional), and was thus unable to account for the effects of local temperature and flow fields. In addition, Verrill and Wessel [7] developed a 3-D CFD (computational fluid dynamics) model that focused on the alkali release and the subsequent fume yield. This model was further developed by Wessel and Baxter [8] to include alkali-salt deposition as well. However,

Fig. 1.1: Fume deposits in the boiler bank (courtesy of H. Tran).

the model did not include the particle dynamics for nucleation, condensation, and coagulation. Since the development of these models, computational power has increased significantly, and the capabilities of CFD have also improved. Indeed, CFD modeling has been used extensively in boiler design for several decades, but most of the recovery boiler CFD models have simulated combustion, heat transfer, and flow field. There has been a lack of a model that combines the capabilities of CFD, fine particle dynamics, and advanced equilibrium chemistry.

The fume particles of the recovery boiler have been studied less extensively than the larger fly ash particles, but there can be substantial fume deposit growth in the superheater, boiler bank, and economizer areas of the boiler. It has been reported that the fine fume particles constitute around 60% of the total particle mass at the superheater area [9], although this amount varies from boiler to boiler. Since fume deposits have a significant role in recovery boiler plugging, there is a need for boiler models that can link the furnace conditions to fume formation and fouling [10]. The need for the modeling of fume formation and chemistry in the recovery boiler has also been identified by Hupa et al. [11].

The objective of this thesis is to present a CFD model developed for the simulation of the alkali metal (Na and K) compounds and the formation of the fume particles and deposits. The model is 3-D, and takes into account both the effect of temperature and flow fields when simulating the gas-particle equilibrium. The effects of mass transfer phenomena and chemical reactions on fume particle formation are also considered. Additionally, the model simulates both the direct condensation of gases on the superheater surfaces and the condensation of gases to fine fume particles, making these two processes compete with each other. Mechanisms for fume particle deposition are also included. This work does not consider the simulation of the larger particles, called carryover, which are mostly fragments of unburned black liquor and do not originate from the alkali metal vapors, as does fume.

The model presented here enhances the coverage of the CFD modeling in recovery boilers, and assists boiler design by improving the understanding of fume formation and deposition mechanisms. The model is not a stand-alone model, and thus it needs to be combined with existing recovery boiler geometries and models for black liquor combustion. At present, the model has only been validated for one recovery boiler in Finland, and new validating tests are needed to obtain more reliable results. However, even at this stage, the model can be used for sensitivity analysis since it can simulate how certain changes in flue gas temperature or black liquor composition, for example, affect the behavior of the alkali metal compounds. This type of information is important in the various design stages of new recovery boilers, such as optimizing sootblowing or selecting the materials used in the heat transfer surfaces.

This thesis has been organized in the following way: Following the introduction, Chapter 2 describes the recovery boiler technology, the chemistry of the alkali metals, and the earlier CFD modeling conducted in the recovery boiler. Chapter 3 introduces the boiler model used in this thesis, explaining how the chemistry calculations are performed and which models are used to simulate fume particle and deposit formation. The results of the recovery boiler modeling are presented in Chapter 4, where they are also compared with measurements in recovery boilers. Chapter 4 also includes the results of the model sensitivity analysis, which examines the most important factors affecting fume deposition in the boilers. The thesis ends with summary, conclusions and suggestions for future work in Chapters 5 and 6.

Chapter 2

Background

2.1 Kraft recovery boilers

The principle of the kraft recovery boiler was patented in the 1930s [12]. Recovery boilers were first invented because the chemicals used in cooking pulp were so expensive that it was necessary to recycle them instead of discarding the black liquor, the waste stream of the pulp cooking process. The kraft recovery boiler fulfilled this need by acting as a chemical reactor that both separates the inorganic chemicals and combusts the organic material of black liquor to produce energy. Despite the age of the technology, recovery boilers still play a vital role in the pulp-making industry. Globally, about 630 recovery boilers are currently in use [13].

In Finland, recovery boilers are also a significant source of renewable energy. In 2012, 31% of the renewable energy and 9.9% of the total energy consumption in Finland originated from the forest industry waste streams [14], which are mostly black liquor [15]. Black liquor will also have a significant role in future energy production because the European Union has set goals for renewable energy production in 2020. According to these goals, Finland should satisfy 38% of its energy needs from renewable sources [16]. This was almost achieved in 2012, the year when wood-based fuels first became the most common energy source in Finland [14].

The recovery boiler is the largest item of equipment in the pulp production line, and its operational reliability is crucial for the entire pulp making process. At present, the largest operating recovery boilers burn 7,000 tons of dry solids a day (t_{ds}/d) [17], but recovery boilers burning 12,000 t_{ds}/d have been planned [18]. Next follows a brief description of the pulping process and the recovery boiler principle, which is based largely on works by Adams [19] and Vakkilainen [20].

The wood entering the pulping process first undergoes cooking, where the chemicals Na_2S and NaOH separate lignin from cellulose. After cooking, the pulp is washed. The waste washing liquid, black liquor, contains lignin and the expended cooking chemicals. The black liquor has high water content and must

Table 2.1: Typical softwood kraft black liquor composition [19].

Element	C	H	S	O	N	Cl	Na	K	Inert
Wt-%	35	3.3	4	35.7	0	0.6	19.7	4	0.1

be evaporated to allow its combustion in the recovery boiler. Nowadays, black liquor is evaporated to a dry solid content of 80 to 85%, when earlier it was usually evaporated only to 65%. The higher heating value of black liquor is relatively low, 13 to 15 MJ/kg_{ds}, mainly because of its high ash content. A typical softwood kraft black liquor composition is shown in Table 2.1.

In the recovery boiler, the black liquor is sprayed into the furnace through special nozzles. The aim is to form droplets which should dry but not completely burn before they reach the char bed at the bottom of the furnace. The char bed consists of carbon, partially pyrolyzed black liquor solids, and smelt. Smelt literally means "molten rock" [21], and in the recovery boiler this consists of molten salts. The char bed must provide a reducing environment for the lower furnace, whereas the upper furnace must remain in an oxidizing environment. The recovery boiler has a dual role, as already mentioned. The organic part of black liquor is combusted in the oxidizing environment, producing heat for steam production. At the same time, all sulfur should be reduced to Na_2S and be recovered from the furnace together with Na_2CO_3, which is the reacted form of NaOH. These chemicals are recovered via smelt, which flows out of smelt spouts located at the bottom of the furnace.

A kraft recovery boiler has various types of heat transfer surfaces, an example of which is shown in Fig. 2.1. At the beginning of the steam-water cycle, economizers are used to preheat the water, which later turns into steam in the boiler (or the generating) bank. Next, the superheater surfaces superheat the steam. The screen is not a necessary part of the boiler, but it is often used to cool the flue gases and to prevent excess carryover and radiation entering the superheater area. Typically, the total heat transfer area in the recovery boiler is larger than in power boilers, because the recovery boiler surfaces are easily fouled, which increases resistance to heat transfer. The fouling is caused by the large amount of ash in black liquor. In order to prevent fouling of the heat transfer surfaces and plugging of the flue gas passages, the spacing between the superheater tube panels is sometimes made wider, though this results in increased boiler size and cost. Another way to prevent fouling and plugging is to increase the frequency of sootblowing, which entails the removal of deposits from the heat transfer surfaces, typically by blowing steam. However, sootblowing is expensive, as it can consume 5–12% of the total steam production [22].

The ash in black liquor also makes the recovery boiler surfaces susceptible to corrosion since, according to Skrifvars et al. [23], even small amounts of chlorine in a salt cause corrosion at the temperatures reached in a typical superheater in the recovery boiler. It has been necessary to limit the steam temperatures and pressures in recovery boilers to relatively low values. Nowadays, the typical highest steam temperature is 515 °C [5], but the increasing demand for electricity production will require even higher temperatures. Increasing the steam values is

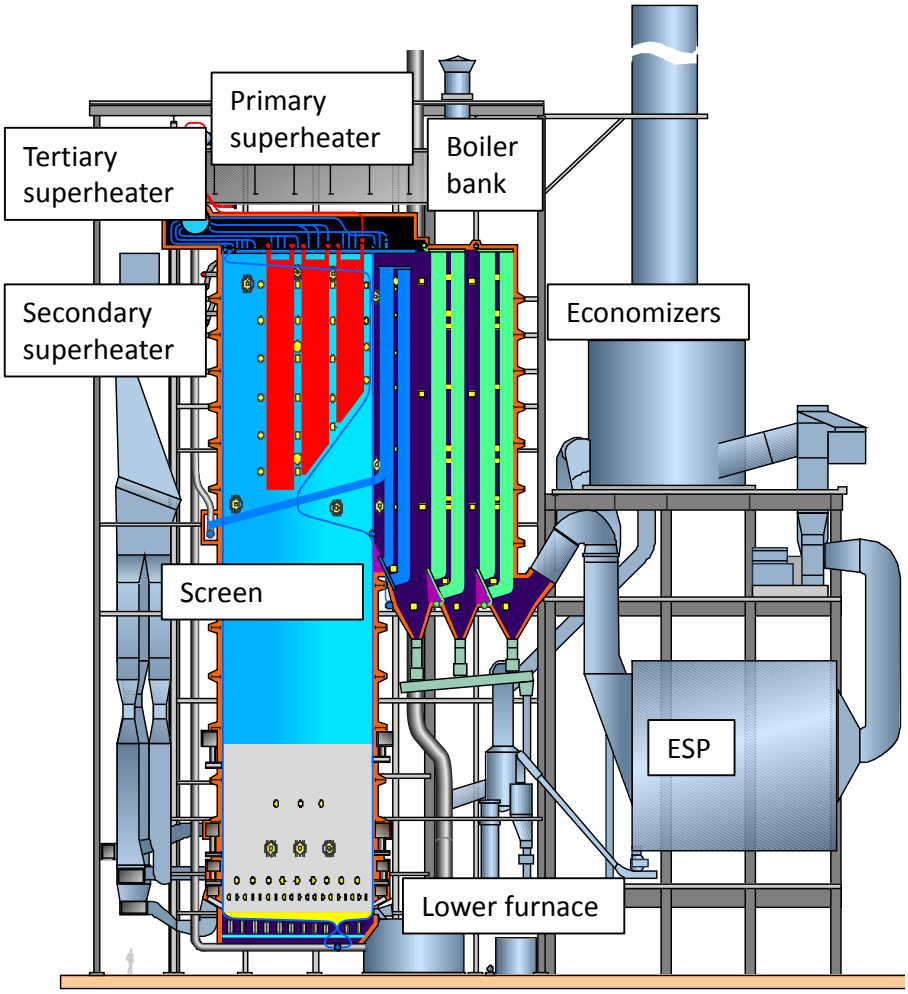

Fig. 2.1: Heat transfer surfaces in a recovery boiler (courtesy of Valmet.)

usually possible only by using more corrosion resistant materials, but they are also more expensive. In addition to higher steam values, another way to increase boiler efficiency is to evaporate black liquor to a higher solids concentration before feeding it to the recovery boiler. This can, however, increase the volatilization of the ash-forming elements, raising the risk of fouling and corrosion. Moreover, attempting to minimize chemical losses by recirculating the boiler ash leads to an accumulation of non-process elements, such as potassium and chlorine. The ash-forming elements are discussed in the following chapter.

2.2 Ash-forming elements of black liquor

Around 30% of black liquor consists of the ash-forming elements sodium (Na), sulfur (S), potassium (K), and chlorine (Cl). Sodium and sulfur originate from the chemicals used in pulp cooking, whereas potassium and chlorine are non-process elements. The potassium and chlorine concentrations in black liquor vary significantly from boiler to boiler, depending on the source of wood and on the chemicals used in different parts of the process. The high variability of black liquor composition between different boilers means that the liquor composition should be taken into account in the design phase of each boiler.

Although the objective in the recovery boiler operation is to recover the used cooking chemicals (Na_2S and Na_2CO_3) via smelt, the volatilization of some of the ash-forming elements to the flue gases cannot be prevented. The ash-forming elements are mainly released from the burning black liquor droplets, and only 5 to 10% of the release occurs from the char bed [24]. The fraction of the elements released depends on several factors, such as the lower furnace temperature and the stability of the flow and temperature field [25]. The release of sodium, potassium, and chlorine increases as the temperature increases, whereas the release of sulfur decreases [26]. On the basis of experiments on wood combustion, chlorine also seems to increase the release of the alkali metals through the formation of alkali chlorides [27]. However, there are currently no simple quantitative correlations for the release in full-scale boilers; the existing models for release have often been validated only in lab-scale reactors and require knowledge of the droplet burning process [7, 26].

The volatilized compounds turn rapidly into alkali (Na or K) hydroxides and chlorides in the high temperatures of the lower furnace [2]. After that, the following global reactions are possible (the reactions are presented here for sodium, but they hold for potassium as well):

$$2\ \mathrm{NaCl} + \mathrm{SO_2} + \mathrm{H_2O} + \tfrac{1}{2}\mathrm{O_2} \rightarrow \mathrm{Na_2SO_4} + 2\ \mathrm{HCl} \tag{2.1}$$

$$2\ \mathrm{NaOH} + \mathrm{SO_2} + \tfrac{1}{2}\mathrm{O_2} \rightarrow \mathrm{Na_2SO_4} + \mathrm{H_2O} \tag{2.2}$$

$$2\ \mathrm{NaOH} + \mathrm{CO_2} \rightarrow \mathrm{Na_2CO_3} + \mathrm{H_2O} \tag{2.3}$$

It can be assumed that most of the alkali metal reactions occur in the gaseous phase because reactions in the molten phase are much slower. In addition, the

condensed alkali chlorides can be sulfated (Eq. 2.1), though Pyykönen and Jokiniemi [28] have reported that the transport of gaseous SO_2 to the deposit surface sets a limit on the sulfation of chlorides in deposits. In modern boilers, the SO_2 is often consumed before the alkali chlorides condense so that no sulfation of the alkali chloride deposits is actually possible.

When the flue gases cool, the volatilized ash-forming elements condense into submicron-sized particles. This volatilized-condensed mode of particles in the recovery boiler is called *fume*. A larger mode ($>$ 100 µm) of particles is called *carryover* and consists of fragments of unburned black liquor or smelt. A third significant particle mode between fume and carryover are intermediate size particles (ISP) [29, 30], though in this work these are classed as carryover.

The concentration of the fume particles in the recovery boiler is 10 to 25 g/Nm^3 [9]. According to the SEM (scanning electron microscope) measurements of Mikkanen et al. [31], the fume particle sizes at the furnace and at the boiler exit are 0.1–0.4 µm and 0.3–0.7 µm, respectively. The main compound in the fume particles is Na_2SO_4, which is also the first compound to condense in the recovery boiler [2]. Additionally, the fume particles contain Na_2CO_3 and NaCl, together with the corresponding potassium compounds. In contrast to fume, the main compound of the carryover particles is usually Na_2CO_3 because their composition reflects the composition of smelt. Some of the volatilized compounds may also condense on the carryover particles, though not in significant amounts since the total surface area of the carryover particles is small compared with the fume particles, especially in the superheater area [32].

The significant size difference between the two main particles modes, fume and carryover, requires different simulation approaches. For example, particle inertia can be ignored for the transport and deposition of fume particles, but not for carryover. The carryover particles deposit mainly by means of inertial impaction and turbulent eddy impaction, whereas the fume particles deposit by diffusion and thermophoresis [33, 34]. In addition to particle deposition, the alkali metal compounds may transfer to surfaces by direct vapor condensation.

2.3 CFD modeling of recovery boilers

CFD modeling of kraft recovery boilers started in the 1980s and 1990s as a result of work by Grace et al. [35] and Karvinen et al. [36]. Most of the recovery boiler CFD models have been used to model combustion, heat transfer, and flow field. For example, air injection strategies [37] and the evolution of the char bed [38] have been investigated. Some research has also focused on modeling the transportation of carryover particles and their deposition on surfaces in the recovery boiler [39, 40], but most research has dealt with particle simulation in power boilers, such as [41, 42]. A recent review by Weber et al. [43] sets out the challenges of predicting the behavior of larger ash particles. The modeling of submicron-sized particles has, however, received less attention. The deposition of submicron particles in biomass combustion (apart from black liquor) has, for example, been modeled by Jöller et al. [44].

To the author's knowledge, the fine particle dynamics of submicron-sized fume particles in a recovery boiler have so far only been modeled by Jokiniemi et al. [2]. These authors developed a model called ABC (Aerosol Behavior in Combustion), which employs a discrete nodal point method to describe the particle size distribution, and couples local chemical equilibrium with aerosol formation [1]. However, due to the limited computational power at the time, the model was 1-D and could only model the parameters as a function of a predetermined temperature change, and not of local temperature or flow field. The same research group later developed a 2-D CFD model based on the sectional method that was used to model a small boundary layer area on a superheater surface [28].

Verrill and Wessel [7] and Wessel et al. [45] have also simulated the amount and composition of fume, but their model did not consider fine particle dynamics, which might have caused inaccuracy in predicting the fume particle composition at different locations in the boiler. Instead, their model focused on predicting the release of Na, K, and Cl through carbonate reduction and alkali chloride vaporization. The release of these elements has also been modeled by Wåg et al. [26], and both of these models were able to accurately predict the sodium release in lab-scale reactors. Subsequent work by Wessel and Baxter [8] and Wessel et al. [30] simulated alkali-salt deposition and, in addition to fume particles, they investigated the deposition of ISP and carryover. These studies utilized multiphase chemical equilibrium calculations, however, recent chemical thermodynamic databases for the recovery boiler environment have seen further development (see Chapter 3.2).

Chapter 3

CFD model for alkali metal compounds and fume particles

3.1 Temperature and flow field

CFD modeling in the present work is performed using the commercial software ANSYS Fluent [3], which is based on the finite-volume method of discretizing the transport equations for mass, momentum, and energy transfer. The general form of the transport equation in the steady state [46] is

$$\frac{\partial(\rho u_j \phi)}{\partial x_j} = \frac{\partial}{\partial x_j}\left(D_\phi \frac{\partial \phi}{\partial x_j}\right) + S_\phi, \tag{3.1}$$

where ϕ is any conserved intensive property. For mass, it is 1, for momentum conservation u_i, and for energy h. The symbol D_ϕ is the effective diffusion coefficient and S_ϕ the source term for ϕ. The term on the left hand side of the above equation represents convection, the first term on the right hand side diffusion, and the second one source terms, such as the gain or loss of the scalar by reactions. For information on how to discretize the different conservation equations, see [47].

In this work, the simulations are time-independent because the alkali metal reactions and the formation of the fume particles are assumed to occur faster than changes in the flow field. The steady-state Reynolds-averaged Navier–Stokes (RANS) equations are used to model all turbulent quantities, and a pressure-based steady-state solver is used in the CFD simulations. Turbulence is modeled with the realizable $k-\varepsilon$ model with standard wall functions, and the turbulence-chemistry interaction with the finite-rate/eddy-dissipation concept. The radiative heat transfer is modeled with the discrete ordinates model, and the pressure-velocity coupling with the SIMPLE scheme. The equations are solved with second-order discretization. More information on the use of the solver can be found in [3].

In the recovery boiler model presented here, the focus is on the formation of fume particles and deposits, which are heavily dependent on the temperature field

in the boiler. It is important, therefore, to obtain a realistic temperature distribution with the simulations, and this is ensured by comparing the modeled temperature distribution with temperature measurements (see Chapter 3.5). Before the reactions of the alkali metal compounds and the formation of the fume particles and deposits are modeled, the temperature and the flow fields are "frozen". In other words, there is a one-way coupling between these fields and particle formation. Because the mass fraction of the ash-forming compounds in the flue gas is below 1%, the processes of particle formation, such as the heat release due to condensation, are not assumed to affect the energy and flow equations.

When black liquor is injected into the recovery boiler furnace through nozzles, it forms droplets, and the trajectories of these droplets are modeled with the Discrete Phase model (DPM) of ANSYS Fluent. In practice, black liquor undergoes four stages during combustion: drying, devolatilization, char burning, and smelt coalescence [48]. The combustion process is fairly complicated, but since the droplet behavior is not the focus of this work, a simplified combustion model is used. However, the models for black liquor droplet injection and black liquor combustion are not developed in this work, but are based on a model employed in the industry [49]. In this model, the pyrolysis of black liquor droplets releases a fraction of the elements into a gaseous form. This modeled release is the sum of the different release mechanisms, and it also includes the release that occurs during char burning. Char burning and smelt coalescence are not modeled as such, nor is the char bed. For char bed modeling, see [38].

In the combustion model used here, the gases CH_4, CO, and H_2 are released during pyrolysis and combusted in the boiler furnace. The combustion reactions release energy according to the reaction enthalpies, though in practice, energy is also consumed by certain reactions that are not modeled, such as sulfur reduction. Thus the amount of released energy has to be adjusted by a correction factor, which is based on the difference between the measured and the calculated heating value for the modeled black liquor. Further corrections to the resulting temperature field can be made if measured temperature values are available.

In terms of the present work, the release of the ash-forming elements is important. The model assumes that Na, K, S, and Cl are released only from the black liquor droplets, and not from the char bed. However, as stated in Chapter 2.2 , the release factors of these elements (i.e., the fractions of the elements entering the gas stream) vary from boiler to boiler, and the actual release factors are difficult to determine. In this work, the release factors (Table 3.1) are based on the measurements of Tamminen et al. [50] and Mikkanen et al. [31, 51, 52]. These values are based on the difference between the amount of the elements in the as-fired black liquor and in the dust entering the ESP (electrostatic precipitator). Although the constant release factors used in this work are simplifications, they are subsequently shown to be realistic because of the good correspondence between the modeled and measured fume particle composition (Table 4.1, p. 40). Nevertheless, a submodel for the release of the ash-forming elements should be developed in the future. Recently, Kangas et al. [53] developed a constrained free energy method for calculating the released amounts of Na, K, S, and Cl, and Jukola et al. [54] suggested that sodium release could be simulated on the basis of

Table 3.1: Release factors used in the model.

Element	Na	K	S	Cl
Release-%	12	17	18	34

the equilibrium vapor pressure of sodium hydroxide. However, these approaches have yet to be adopted here.

In the model, the ash-forming elements are assumed to be released in the form of KCl, KOH, NaCl, NaOH, and SO_2. In practice, sulfur is released mainly in the form of H_2S, but it is quickly oxidized to SO_2. In the boiler furnace, the released ash-forming elements react to form alkali sulfates, carbonates, hydrogen chloride, and water according to the global reactions described in Chapter 2.2 (Eq. 2.1–2.3, p. 7). These reactions are modeled as equilibrium reactions, as explained in the next chapter.

3.2 Equilibrium chemistry

In this work, the formation of the alkali metal compounds occurs according to the global reactions presented in Chapter 2.2, but no kinetic rates for the reactions are given. Instead, the reactions are modeled as equilibrium reactions. The reactions are assumed to reach equilibrium because the temperature in the recovery boiler is relatively high, and the residence times of the alkali metal compounds are approximated for long enough to allow equilibrium to be reached. The equilibrium assumption has also been used by Jokiniemi et al. [2], Wessel and Baxter [8], and Kangas et al. [53] in the upper furnace of the recovery boiler, and by Saw et al. [55] for black liquor combustion in a flat flame. When using the equilibrium approach, perfect mixing is assumed.

The states of the equilibrium reactions are calculated using the Equilib module of the thermodynamic software FactSage [56]. FactSage has several databases for chemical compounds, of which FTsalt [57] contains data for salt systems, and FTpulp [58] is specifically compiled for use in the recovery boiler environment. Calculating the chemical equilibrium in Equilib is based on the minimization of Gibbs energy G, which is

$$G(T) = \Delta H_{T_0} + \int_{T_0}^{T} C_p(T)dT - T \cdot \left(S_{T_0} + \int_{T_0}^{T} \frac{C_p\,(T)}{T} dT \right), \qquad (3.2)$$

where T_0 stands for the standard temperature of 298 K [59]. In the Gibbs energy minimization method, the sum of the Gibbs energies of all possible components and phases will be minimized. For given conditions, the method gives the combination of components and phases that provide the minimum sum of the Gibbs energy.

In order to shorten the time required for the CFD simulations, the equilibrium calculations are not conducted during the simulations. Instead, a spreadsheet is precalculated with the equilibrium software, and used in the CFD calculations by

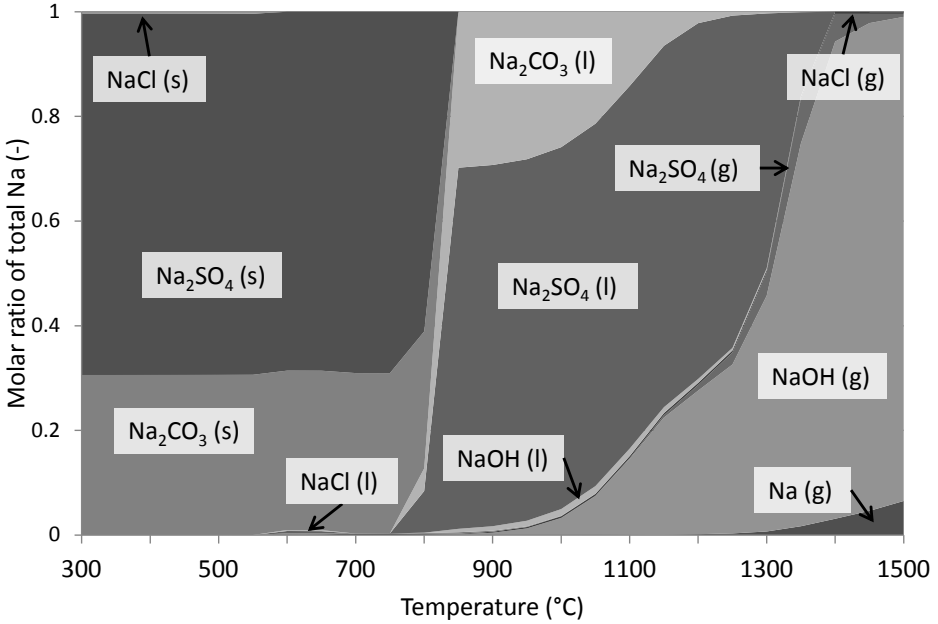

Fig. 3.1: Sample result of an equilibrium calculation showing how Na distributes between different compounds. The initial mass fractions are shown in Table 3.2.

an iterative method. The spreadsheet values are calculated by varying the flue gas temperature and the mass fractions of Na, K, S, and Cl in the equilibrium calculations and finding out the state of each global equilibrium reaction (Eq. 2.1–2.3, p. 7). In CFD modeling, on the other hand, the local values of these variables in each computational cell determine which values are interpolated from the spreadsheet. The modeled average values of the mass fractions of H, C, N, and O are used in the equilibrium calculations. The spreadsheet values are calculated for oxidizing conditions because the main area of interest is in the superheaters where the oxidizing conditions prevail. As a consequence, the model is not capable of predicting the chemical conditions in the reducing environment of the lower furnace.

A sample result for an equilibrium calculation is shown in Fig. 3.1. The figure presents the various compounds containing sodium (as molar ratio of total Na). Table 3.2 shows the initial mass fractions of the elements used in the calculation, which correspond roughly to the average mass fractions in the flue gas of the second boiler modeled in this work. It is noteworthy that the fraction of NaCl is very low in the presented simulation because the black liquor burned in the modeled boiler had unusually low chlorine content.

Only the main sodium-containing compounds are labeled in Fig. 3.1. It can be seen that most of these compounds exist in three phases: gas, liquid, and solid. It is also important to note that the compounds do not melt instantly at one temperature. For example, there is both solid and liquid Na_2CO_3 present at

Table 3.2: Initial mass fractions used in the equilibrium calculation in Fig. 3.1.

Element	Cl	K	S	Na	H	C	O	N
Mass fraction (-)	$2 \cdot 10^{-5}$	$2 \cdot 10^{-4}$	0.0015	0.003	0.014	0.06	0.29	0.64

800 °C. This is typical for mixtures of chemical compounds, which often have a first melting temperature, a complete melting temperature, and a state between these two extremes when the mixture is partly molten [33]. The actual melting temperatures depend on the composition of the mixture.

For simplification, the alkali metal reactions in the CFD modeling proceed only when the reactants are in the gaseous form because the reactions in the molten form would be challenging to model due to slow diffusion. However, the assumption of the gas-phase reactions does not invalidate the simulation of the chemical equilibrium because all possible phases of the alkali metal compounds are considered when the chemical equilibrium is calculated. In the modeling, the fine particle dynamics determine when the alkali metal compounds move from the gas phase to the particle phase, which, in this work, combines the liquid and solid states of the condensing compounds.

The validity of the equilibrium chemistry assumption could be criticized on the grounds that the sulfation of alkali chlorides (NaCl and KCl) can be kinetically limited. Christensen et al. [60] claim that under the equilibrium assumption in their simulations of straw combustion, the sulfation of KCl was significantly overestimated. They assumed that residence times in the boiler were not long enough for the sulfation reaction to reach equilibrium, but no further information was given on the residence times or the temperature distribution used in their simulations. Other articles have used approximately 800 °C as a limit above which the sulfation of KCl would not be kinetically limited [44, 61]. No such limit is used in the present work. The equilibrium calculations show that most of the reactions occur above the critical temperature of 800 °C, since at least 95% of Na_2SO_4 forms at temperatures above 1150 °C, and at least 95% of K_2SO_4 forms at temperatures above 850 °C. Thus using the equilibrium assumption for the sulfation reactions seems justified.

3.3 Fine particle dynamics

In order to consider the mass transfer limitations and the supersaturation requirement in the formation of fume particles, the fine particle dynamics must be simulated. Here, the simulation of fine particle formation, growth, and movement is based on the commercial Fine Particle Model (FPM) software [4]. This model was chosen because incorporating aerosol dynamics into a CFD program lay outside the focus of this thesis. Furthermore, the FPM has a graphical user interface and it uses a method which enables the simulation of very large particle populations. It has been used earlier in the simulation of vehicle particle emissions [62], nucleation [63, 64, 65], and $PbCl_2$ transformation in a bench-scale

reactor [66]. As far as is known, no research project, apart from the present one, has applied the FPM to a full-scale boiler. The FPM is intended for simulating the formation of particles below 10 µm in diameter, which is a suitable range for the modeling of fume particles when carryover is excluded.

Carryover particles are not modeled in this work because they form by a completely different mechanism compared to fume. Carryover consists mostly of fractions of unburned black liquor or smelt, and the size of the carryover particles is above 100 µm [33]. Because of the large size and the relatively small number of the carryover particles, they cannot be modeled by the Eulerian approach, but instead, by Lagrangian particle tracking. Moreover, the total surface area of the carryover particles is small compared with the total surface area of the fume particles, which causes most alkali metal vapors to condense on the fume particles [32]. Carryover deposition may be significant at the beginning of the superheater area, but because of their larger size, most of the carryover particles are unable to travel far in the area. Since the research focus here is on the superheater and the boiler bank, neglecting the modeling of carryover deposition seems justified. Moreover, research into carryover dynamics has been conducted elsewhere [39, 40].

In contrast to the discrete particle model in the CFD software, the FPM models the particles in the Eulerian reference frame. This means that the particle populations are treated as gaseous species, which enables the efficient simulation of very high particle concentrations. The FPM uses the modal aerosol dynamics (MAD) approach for representing the particle size distributions [67, 68]. In the MAD approach, the particle populations are divided into modes which each have an analytical modal distribution function. In the FPM, a lognormal distribution is assumed since this has been found applicable to most single-source aerosols, although no theoretical explanation for this has been given [34]. The lognormal density function of mode j [68] is

$$n_j(m_p) = \frac{N_j}{\sqrt{2\pi} m_p \ln \sigma_{g,j}} \exp\left(-\frac{(\ln m_p - \ln m_{gn,j})^2}{2 \ln^2 \sigma_{g,j}} \right), \tag{3.3}$$

which is characterized by three unknown parameters: the total number concentration N_j, the geometric mean mass $m_{gn,j}$, and the geometric standard deviation $\sigma_{g,j}$.

For each of the particle modes, the FPM solves differential equations for three integral moments to find the values of three unknown parameters. The k^{th} moment of the distribution of mode j [68] is

$$M_{k,j} = \int_0^\infty m_p^k n_j(m_p) dm_p. \tag{3.4}$$

The mode $M_{0,j} = N_j$ in Eq. 3.4. Finally, the solved moments are substituted in the general dynamic equation (GDE) for aerosols. For more information on this, see [68, 4]. The general form of the GDE for the discrete distribution function [69] is

$$\frac{\partial n_l}{\partial t} + \nabla \cdot n_l \mathbf{v} = \nabla \cdot D \nabla n_l + \left[\frac{\partial n_l}{\partial t}\right]_{growth} + \left[\frac{\partial n_l}{\partial t}\right]_{coag} - \nabla \cdot \mathbf{c} n_l, \qquad (3.5)$$

where l refers to the number of molecules in the particle. In the above equation, the first term on the left hand side stands for time dependency, and the second for convection. On the right hand side, the first, second, third, and fourth terms represent diffusion, particle growth, coagulation, and the effect of external forces on the particle velocity, respectively. Through the GDE, the FPM is able to account for the changes in the size distributions caused by convective transport, diffusion, coagulation, particle growth due to condensation and nucleation, as well as external forces such as sedimentation and thermophoresis.

In addition to assuming a lognormal distribution function for the particles, other assumptions have been made in the FPM [4]. The particles are assumed to be spherical because most condensed compounds are in the molten phase when they form. Since the particles are small, the particle temperature is assumed to be uniform and equal to the temperature of the surrounding flue gas. Particle inertia is also neglected due to the small size of the particles. Additionally in this work, the particles are assumed to form only one mode to shorten the time used for the computations.

The moment method used in the FPM is considered suitable when the characteristic shape of the particle distribution is known [67], and this is usually the case when simulating aerosols in combustion. However, there are alternatives to the moment method presented here. Pyykönen [70] finds that sectional methods are more accurate than moment methods, but in practical cases when many other uncertainties exist, the difference in accuracy is insignificant. Moreover, the sectional methods require more computational power because the particle size range must be discretized into sections, the number of which can be high if the size distribution is wide.

Equilibrium vapor pressure functions

The equilibrium vapor pressure of a chemical compound is an important parameter in the fine particle dynamics. It represents the pressure where the vapor is in thermodynamic equilibrium with its condensed phase in a closed container, that is, the rates of evaporation and condensation are equal. The equilibrium vapor pressures are highly dependent on the temperature of the system, and therefore represented as functions. Figure 3.2 presents the equilibrium vapor pressure functions of certain pure compounds that are important in this thesis. According to the references, the functions for KCl and NaCl are valid above 800 °C [71], for K_2SO_4 above 600 °C [72], and for Na_2SO_4 above 900 °C [71], but the functions are extended below these values in order to model condensation in the whole superheater area. This assumption is not considered to cause a significant error since, according to the modeling results, Na_2SO_4 and K_2SO_4 condense well above 1000 °C, and most of NaCl and KCl above 800 °C. The vapor pressures in Fig. 3.2 are shown on a logarithmic scale.

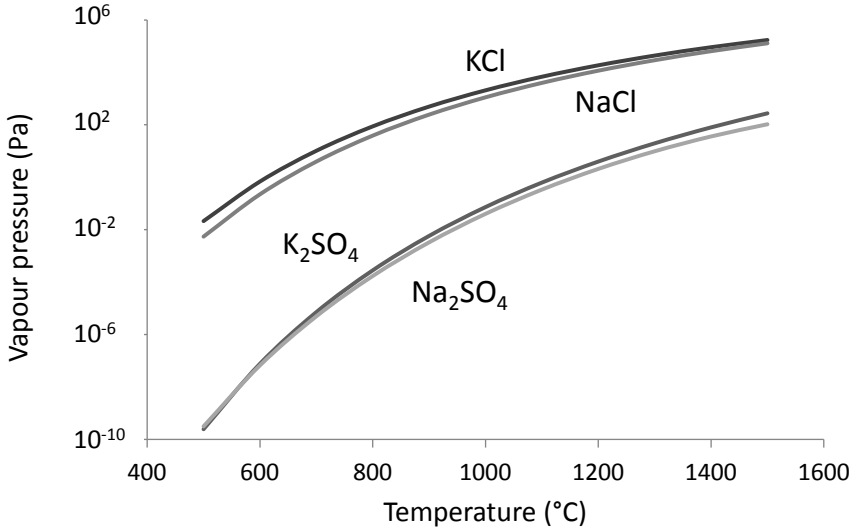

Fig. 3.2: Equilibrium vapor pressure functions of some pure alkali metal compounds [71, 72].

Figure 3.2 shows that the equilibrium vapor pressures of the alkali chlorides NaCl and KCl are much higher than for the alkali sulfates. In practice, this means that the alkali chloride vapors need lower temperatures to shift their equilibrium towards the condensed phase. The alkali sulfates, on the other hand, start condensing at relatively high temperatures. The functions for the alkali carbonates are not shown in the figure because, according to the equilibrium calculations conducted in this work, gaseous alkali carbonates should not exist and thus they are assumed to condense as soon as they form.

Formation of particle nuclei

The fine particle dynamics is governed by the saturation ratio S_i, which is the partial pressure of a vapor divided by its equilibrium vapor pressure at the prevailing temperature. The following equation gives the saturation ratio for pure compounds:

$$S_i = \frac{p_i}{p_{i,S}\left(T\right)}. \tag{3.6}$$

If S_i is above one, the vapor is supersaturated. Supersaturation can be caused by the vapor cooling, or by the formation of a new chemical compound which has a lower equilibrium vapor pressure than the original compound. An example is the formation of alkali sulfates from alkali chlorides.

Supersaturation is not thermodynamically favored, and a supersaturated vapor usually nucleates to form a new particle, or condenses on already existing particles or surfaces. *Homogeneous nucleation* occurs if molecular clusters of a

vapor exceed the critical size required for homogeneous nucleation (for more information, see [69]). The critical size is affected by the Kelvin effect, in which the partial pressure required for mass equilibrium is higher for a curved than for a flat surface [34]. The nucleation rates are very sensitive to surface tension values [60], and the nucleation models should be adjusted with empirical correction factors [70]. The FPM contains models for nucleation rates, such as the Frenkel model [73], but the modeling of nucleation is generally considered uncertain [62, 63]. Moreover, nucleation can cause sharp gradients in the particle moments, which requires a very fine computational grid to avoid the divergence of the CFD solution.

Another reason for the difficulty in modeling of nucleation is the uncertainty over whether particle formation starts as a result of nucleation, or as a result of condensation on inert particle seeds [2, 74]. The seeds could be metal oxides, such as Na_2O, which have such low vapor pressures that they nucleate as soon as they form, even in the high temperatures of the lower furnace. Indeed, Jokiniemi et al. [2] have found metal oxides in the recovery boilers. However, the uncertainty over the initiation of particle formation is not significant since the total mass of the particle nuclei is small and coagulation should smooth the number distribution, irrespective of the origin of the particle nuclei [2, 70]. In this work, an alternative approach to modeling nucleation is to insert a predetermined distribution of inert particle nuclei into the recovery boiler.

Heterogeneous condensation

Condensation on already existing nuclei requires lower supersaturation values than homogeneous nucleation, and is therefore preferred, if nuclei exist [34]. The process is usually called *heterogeneous condensation* because different compounds can condense on the same particle. An opposite phenomenon to condensation, evaporation, may occur if the vapor above a surface becomes undersaturated. The FPM takes into account both condensation and evaporation. These processes are modeled according to the approach of Barrett and Clement [75], which takes into account the saturation ratio (Eq. 3.6) of the vapor and the mass transfer limitations of condensation and evaporation. It is important to include the fine particle dynamics in the modeling of condensation, since the equilibrium calculations alone may not accurately predict the location of fume particle formation [45]. Condensation is an important process, because it determines the total mass and the composition of the fume particles.

When different vapors condense on the same particle, their vapor pressures are often calculated using Raoult's law, which assumes that the partial pressure of a component in an ideal solution is proportional to its mole fraction. This method is adapted in the FPM by assuming that the activity of a condensed compound is equal to its mole fraction in the condensed particle [4]. Eskola et al. [32] have also approximated vapor pressures using Raoult's law and by assuming that the condensing compounds in the fume particles form a molten salt solution. It is possible that the condensing vapors form a mixture that has a lower vapor pressure than any of the compounds individually [70], especially if different types of molten species exist simultaneously. However, taking account of the non-ideal

interactions of the condensed compounds lies outside the scope of this work. In another alternative approach for calculating the vapor pressures, Pyykönen and Jokiniemi [28] model the condensation of NaCl only. The authors assume that the other compounds have solidified when NaCl condenses, and thus they use the equilibrium vapor pressure of pure NaCl. However, they also note that it is not fully clear how the surface composition of the fume particles develops.

Coagulation

In coagulation, particles stick together upon collision and form new spherical particles. The coagulation of solid particles is sometimes called agglomeration [34]. With sufficient time, coagulation develops particle size distributions with a geometric standard deviation of 1.32–1.36 [34]. In most cases, this means that the original particle size distribution becomes narrower since the number of small particles decreases significantly and the number of larger fine particles slightly increases. Furthermore, in industrial boilers, particle number concentrations fall quickly below 10^9 particles/cm^3 due to coagulation [70], which is why the original number of particle nuclei is not very significant. The FPM assumes that the collisions occur between two particles, and uses the Dahneke model [76] for coagulation.

Coagulation is the main process determining the number and size distribution of the fume particles. However, as the number and size of the initial particle nuclei in the recovery boiler is not accurately known, the particle number and size distributions of the condensed fume particles can only be approximated.

3.4 Fume deposit formation

Models for deposit formation are not available in the FPM, but the author has implemented them into the CFD model presented here through user-defined functions (UDF). This work considers only the modeling of fume deposit formation, which covers the deposition of fume particles and the direct condensation of alkali metal vapors. As stated in the previous chapter, the inertia of the fume particles is insignificant due to their small size (< 1 µm), and therefore inertial impaction can be neglected. Turbulent impaction, which is caused by the inability of particles to follow turbulent eddies [28], is also neglected for the same reason. If the deposition of carryover particles is to be modeled, these processes should be taken into account. Another difference from carryover is that the fume particles are assumed to stay on the surfaces where they are transported, whereas the adhesion of the carryover particles is affected by the melting temperatures of the ash in the particles. The carryover particles need to have a melt fraction of 15 to 70% in order for them to stay on the surfaces [77]. Moreover, the carryover particles are approximated to be completely solid at temperatures around 750 °C and below, which means that they should not deposit in the upper superheater area [8].

Thermophoresis

Thermophoresis is generally considered the main deposition mechanism for the fume particles [34]. It has been demonstrated to be the main mechanism of fume deposition in the recovery boiler [78], although opposing experimental results have also been obtained [79] (see Chapter 4.3). In simple terms, thermophoresis is caused by a temperature gradient in a gas because the gas molecules on the hotter side of the particles transfer more momentum, which makes the particles move towards the lower temperatures. The general formula for the thermophoretic velocity [34] is

$$v_{th} = \frac{-K\nu\nabla T_{gw}}{T_{ave}}, \tag{3.7}$$

which is directly dependent on the dynamic viscosity ($\nu = \mu/\rho$) of the flue gas and the temperature gradient between the flue gas (g) and the wall (w), and inversely proportional to the temperature in the vicinity of the particle, which in this case is the average temperature between the flue gas and the wall, T_{ave}. The parameter K is a multiplier, the value of which depends on the model used for thermophoresis.

In reality, the thermal force experienced by the particle is also affected by the thermal conductivities of the gas, k_g, and the particle, k_p. The Talbot interpolation formula [80] takes this into account, and it is commonly used to calculate the value of K_T, which can be substituted for K in Eq. 3.7:

$$K_T = \frac{2C_s\left(\frac{k_g}{k_p} + C_t\frac{2\lambda_g}{d_p}\right)C}{\left(1 + 3C_m\frac{2\lambda_g}{d_p}\right)\left(1 + 2\frac{k_g}{k_p} + 2C_t\frac{2\lambda_g}{d_p}\right)}. \tag{3.8}$$

The equation is also dependent on the mean free path of gas, λ_g, and particle diameter, d_p. The constants C_s, C_t, and C_m are 1.17, 2.18, and 1.14, respectively. The Cunningham slip correction factor is $C = 1+2\lambda/d_p\left[A_1 + A_2\exp\left(-A_3 d_p/\lambda\right)\right]$, where the constants A_1, A_2, and A_3 are 1.257, 0.400, and 0.55, respectively [81].

The challenge in using the Talbot equation is that the particle size and thermal conductivity are often not accurately known, and this brings a source of uncertainty into the calculated thermophoretic velocity. However, when the Knudsen number $\mathrm{Kn} = 2\lambda_g/d_p$ is above one, the effect of particle size is almost negligible and the effect of thermal conductivity is practically insignificant [69]. This is the case in most of the superheater area considered in this work because of the submicrometer size of the fume particles and also the high gas temperatures that increase the mean free path of gas. Lockwood et al. [82] also assume free molecular behavior ($\mathrm{Kn} > 1$) of the combustion products at furnace temperatures. Kær et al. [83] use a thermophoresis function which has particle size as a parameter, but they also note that fine particle deposition is not heavily dependent on the particle diameter as long as it is in the micrometer range.

A simpler alternative to the Talbot equation for the thermophoretic velocity is the Waldmann and Schmidt equation [84], which can be used to calculate the parameter K_{WS} that can be substituted for K in Eq. 3.7:

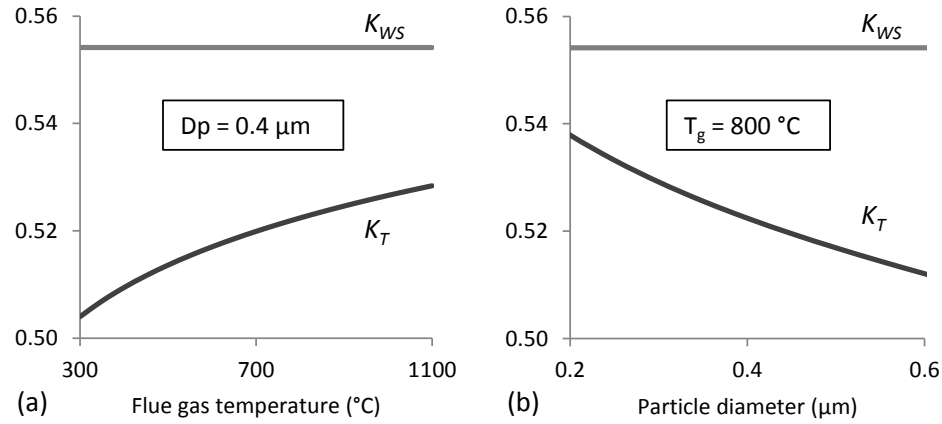

Fig. 3.3: Comparison of the multipliers for thermophoretic velocity by Eqs. 3.8 and 3.9 as a function of temperature (a) and particle diameter (b).

$$K_{WS} = \frac{3}{4\left(1 + \frac{\pi\alpha}{8}\right)}, \tag{3.9}$$

where the accommodation coefficient α is usually given a value of 0.9 [69]. The main drawback of this function is that it is not dependent on particle size or the thermal conductivities of the particle and the gas. However, in the modeled boiler the difference between Eqs. 3.8 and 3.9 is insignificant, as Fig. 3.3 shows. The example calculations are made by estimating that the ratio k_g/k_p varies between 0.02 and 0.05, increasing with the flue gas temperature.

Figure 3.3 (a) shows the factors K_T and K_{WS} as a function of the flue gas temperature when the particle diameter is held constant at 0.4 µm. In the temperature range prevailing at the superheater area, the difference between K_T and K_{WS} is 5–9%. When the factors are drawn as a function of particle diameter with a constant flue gas temperature of 800 °C, the difference is 2–8%, as shown in Fig. 3.3 (b). The differences are smallest at the highest temperatures and with the smallest particle sizes because here the Knudsen number approaches or exceeds one. Despite the slight inaccuracy in the thermophoretic velocity given by Eq. 3.9, it is advantageous in a situation when the particle size is not reliably known, and therefore it is used in this work.

Diffusion

Another important deposition mechanism for fume particles is deposition by diffusion, particularly for particles less than 0.1 µm in diameter [33]. In this work, particle deposition is modeled by an empirical function from Wells and Chamberlain [85]. The function is intended for the diffusive deposition velocity through the laminar boundary layer for turbulent flow in a tube, and it is given as

$$v_{diff} = \frac{0.04 v_g}{\mathrm{Re}^{1/4}} \left(\frac{\rho_g D_p(T_{ave})}{\mu} \right)^{2/3}, \tag{3.10}$$

where $\mathrm{Re} = \rho_g v_g d_c / \mu$, and $D_p(T_{ave})$ the particle diffusion coefficient. In this model, $D_p(T_{ave}) = D_p \cdot T_{ave}/T_0$, where T_0 is the standard temperature of 293 K, and $D_p = 8.31 \cdot 10^{-11}$ m^2/s, corresponding to the diffusion coefficient of an airborne particle under standard conditions when the size of the particle is 0.4 µm [34]. This approximate approach in calculating the diffusion coefficient is shown to be acceptable because deposition by diffusion is later shown to have only a minor role in the fume deposit formation (Chapter 4.3).

Direct vapor condensation

The direct condensation of vapors to heat transfer surfaces is not, strictly speaking, a particle deposition mechanism, but in this work it is considered one method of fume deposit formation. In direct vapor condensation, the supersaturated alkali metal vapors do not first condense on the particles, but directly on the heat transfer surfaces. Modeling direct vapor condensation is important because it is possible that deposits formed by this mechanism have a composition and morphology unlike that of the deposits formed by the deposition of particles. Jokiniemi et al. [86] have noted that alkali chloride vapors, in particular, can condense directly on the heat transfer surfaces, which may increase the chloride content of the deposits in a harmful way.

In this work, the direct vapor condensation flux is modeled by the following equation from Jokiniemi et al. [86]:

$$I_v = \mathrm{Sh}(T_g) \frac{\left[D_v(T_g) D_v(T_w) \right]^{1/2}}{d_c R_u} \left(\frac{p_v(T_g)}{T_g} - \frac{p_{v,S}(T_w)}{T_w} \right), \tag{3.11}$$

where $\mathrm{Sh}(T_g) = 0.023 \cdot \mathrm{Re}^{0.8} \cdot \mathrm{Sc}(T_g)^{0.4}$, and $\mathrm{Sc}(T_g) = \mu / \left[\rho_g D_v(T_g) \right]$. In Eq. 3.11, the characteristic diameter d_c (the distance between the boiler bank tube centers) has replaced the hydraulic diameter d_H in the original equation, because they are of the same order of magnitude and the value of d_H varies in the modeled area. The direct vapor condensation flux is also dependent on the actual vapor pressure of the condensing gas, $p_v(T_g)$, and on the saturation vapor pressure of that gas at the wall temperature, $p_{v,S}(T_w)$.

3.5 Boiler modeling

In this work, two kraft recovery boilers have been modeled. Boiler A (Papers I and II) is in South America with a firing capacity of 5,500 t_{ds}/d hardwood black liquor, and Boiler B (Papers III and IV) is in Finland with a capacity of 3,400 t_{ds}/d softwood black liquor. The black liquor compositions used in the modeling are given in Table 3.3. The chlorine and potassium contents, in particular, are very different for the two boilers.

Table 3.3: Black liquor composition in boilers A and B.

Element	C	H	S	O	N	Cl	Na	K	Inert
Wt-% (A)	33	3.2	6.1	34	0.1	0.6	18	4.0	0
Wt-% (B)	33.5	3.4	6.5	34.5	0.1	0.06	20.8	0.9	0.2

The modeling of the alkali metal compounds and fine fume particles started by considering only the formation of sodium sulfate, sodium chloride, and the corresponding potassium compounds (Paper I). This simplification was made in order to focus on developing the connection between the CFD modeling, equilibrium chemistry, and fine particle dynamics. The formation of sodium and potassium carbonate was subsequently added to the model (Papers II–IV).

Initially, nucleation was modeled according to the Frenkel model (Paper I) with Na_2SO_4 being the only compound able to nucleate since it is the main compound in the fine fume particles [2]. However, the CFD solution showed a tendency to diverge due to the sharp gradients caused by nucleation. The modeling of nucleation was later discarded, and instead, inert particle nuclei were inserted into the furnace (Papers II–IV). The geometric mean diameter of these particles was approximately 0.01 μm, and the initial number concentration about 10^{14} particles/m^3. The assumed size of the diameter of the nuclei is much the same as that assumed by Jokiniemi et al. [2]. In addition, the assumed number concentration reaches the value that, according to Pyykönen [70], should prevent significant supersaturation of alkali metal vapors in the boiler environment. However, the final fume particle mass and composition were unaffected by the insertion of nuclei because the particle nuclei had negligible mass compared with the fume particle mass after condensation. Furthermore, it was found in this work that the fume formation results are almost independent of the number of the inserted particle nuclei. Only the amount of the vapors condensing directly to surfaces might be slightly affected.

The recovery boiler models use two separate geometries: one for the boiler furnace and one for the superheater area. Paper I considers only the modeling of the furnace of Boiler A, whereas Paper II also presents the simulation results in the superheater area of that boiler. Papers III and IV introduce the simulation results for the superheater area of Boiler B. The modeling results for the furnace of Boiler B are not presented because the focus of interest was on fume deposit formation in the superheater area. The furnace of Boiler B was only modeled to obtain the input conditions to the superheater grid.

Boiler furnace

The geometry and the grid used to model the furnace of Boiler A are presented in Fig. 3.4. The geometry of the furnace of boiler B is almost the same, and both geometries are created by Valmet.

The boiler furnace is bound by the furnace walls and the char bed surface, which are modeled using wall boundary conditions. At the top, the geometry extends until the nose arch, where a pressure outlet boundary condition is used.

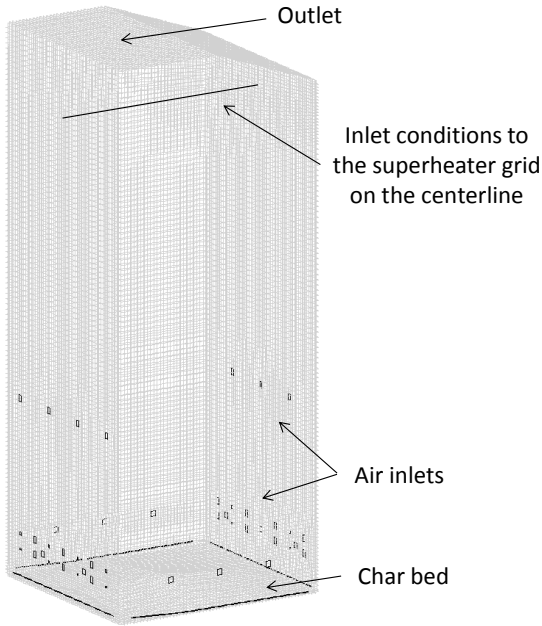

Fig. 3.4: Boiler furnace geometry and grid for Boiler A.

The mass flow inlets for the air and the odorous gases are located at the lower furnace. The trajectories for the black liquor droplets are defined so that the black liquor is injected between the secondary and the tertiary air levels.

The furnace models of Boilers A and B consist of around 400,000 and around 1.0 million cells, respectively. When the modeling results of the furnace are transferred to the superheater grid, the values of the variables on the centerline of a cross section (see the line in Fig. 3.4) are used as input conditions in the superheater grid.

Superheater area

The geometry of the superheater area of Boiler B is shown in Fig. 3.5. The geometry of the superheater area of Boiler A is similar, but not shown here. Again, both geometries were originally created by Valmet. The grid for the superheater area is not shown because it is so dense that individual cells could not be distinguished. The grid consists of around 400,000 cells for Boiler A, and around 800,000 for Boiler B.

The superheater area covers the area from below the nose arch to the boiler (or the generating) bank, but only for a thin cross section of 0.19 m between two superheater platens. Since all cross sections of the superheater area are geometrically similar, the same grid can be extended to different sections in the superheater area by changing only the inlet boundary condition. The inlet flow to the superheater area comes from the simulations in the furnace. The boiler bank is not modeled in its full length, and the economizers and the ESP are not

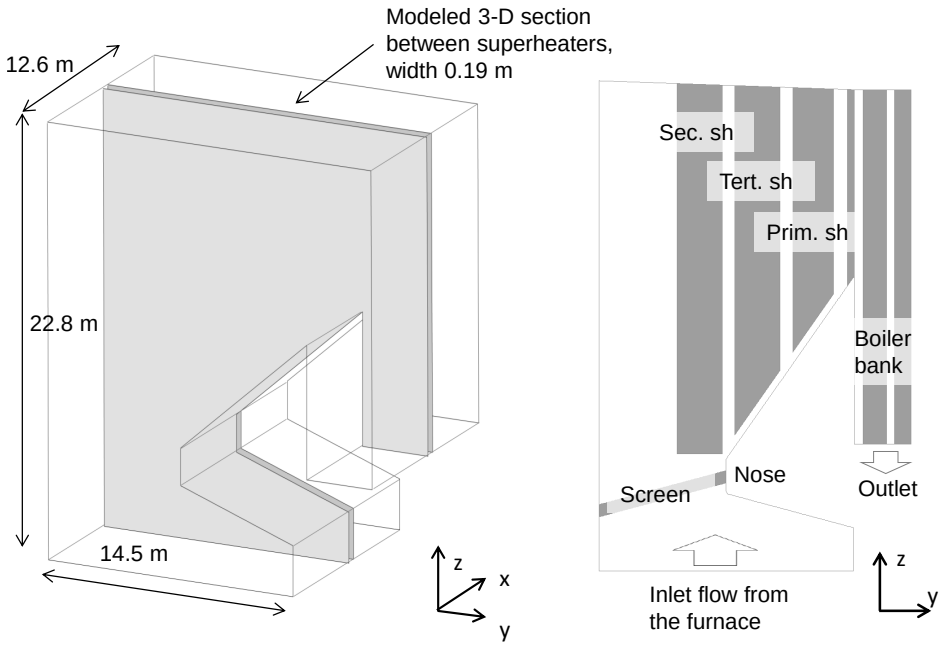

Fig. 3.5: Schematic of the superheater geometry and names of the superheater surfaces of Boiler B (Paper IV).

modeled at all because all alkali metal compounds should condense before the flue gases reach the economizers.

In this work, the modeling of the superheater area is different from that of Wessel et al. [8], where the superheaters were simulated as porous media. The model presented here uses a geometry that includes the superheater platens, which makes it possible to model particle deposition more accurately. The geometry is displayed in Fig. 3.6 , which shows a small area between the tertiary and primary superheaters on the xy-plane (viewpoint from the top of the modeled superheater area in Fig. 3.5). The figure illustrates how the superheater platens are modeled and which area is covered by the computational grid.

In the superheater geometry, the individual boiler tubes are not modeled, but instead, deposits are assumed to fill the cavities between the boiler tubes and to form rectangular superheater platens, as shown in Fig. 3.6. A similar assumption has been made by Pyykönen and Jokiniemi [28]. As the figure shows, the computational grid covers the area between two superheater platens in the areas of tighter tube spacing (the primary superheater and the boiler bank), and half of the area between two superheater platens in the areas of wider tube spacing (the secondary and tertiary superheaters and the screen). Wall boundary conditions are used for the deposit surfaces along with information on the tube surface temperature and the deposit properties. In those areas where the computational grid is bound by the flue gas, the symmetry boundary condition is used.

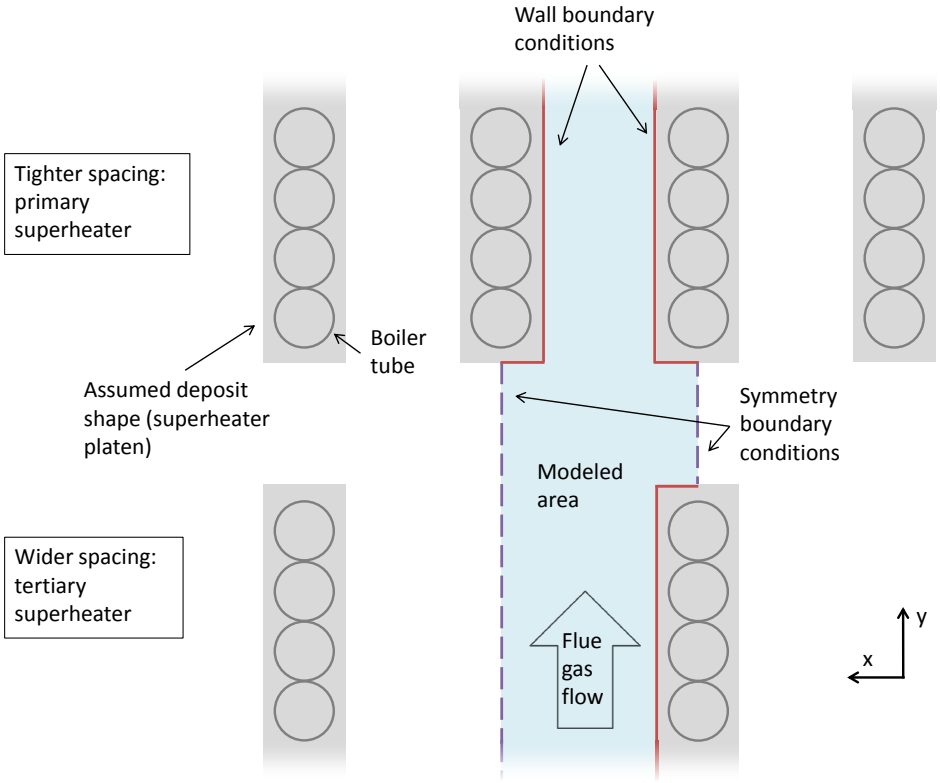

Fig. 3.6: Schematic of the superheater platens between the tertiary and the primary superheater (Paper IV).

In practice, the deposit thickness increases due to the deposition of the particles and decreases due to erosion mechanisms, such as sootblowing. This work, however, presents the results of steady-state modeling, and thus time-dependency of the deposit thickness is not simulated. Instead, certain predefined deposit thicknesses are used, which are assumed to represent typical average deposit thicknesses on the different heat transfer surfaces. This assumption is reasonable since the objective of this study was to simulate how the deposit growth rate and composition are affected by the given boundary conditions. Simulating time-dependent deposit thickness involves changing the computational grid in the middle of the simulations and this would require significant computational resources.

There is no measurement data on the fume deposit thicknesses in the superheater area, so the deposit thicknesses are determined by an indirect method via temperature measurements. The temperature measurements can be used because the deposit thickness affects the heat transfer rate through the deposit, which again affects the flue gas temperature. Those deposit thicknesses that give the best correspondence between the measured and modeled flue gas tempera-

Table 3.4: Tube surface temperatures and deposit thicknesses used as boundary conditions in the model for Boiler B.

Superheater	Screen	Secondary superheater	Tertiary superheater	Primary superheater	Boiler bank
Metal temperature (°C)	316	407	467	343	312
Deposit thickness (mm)	30	48	56	34	21

tures are used in the modeling. Table 3.4 shows the values for the superheater tube surface temperatures and the deposit thicknesses used in the modeling of Boiler B. The values for the tube surface temperature are based on the average values of the steam temperatures in the tubes. The values for Boiler A are not shown because deposit formation was not modeled for that boiler.

In addition to adjusting the deposit thicknesses, the incoming flue gas temperature can also be adjusted. In the modeling of Boiler B, the temperature obtained from the boiler furnace was increased by 50 °C because it resulted in better temperature correspondence. With the chosen values for the deposit thicknesses and the incoming flue gas temperature, the measured and modeled temperatures were within ±60 °C of each other, as shown by Fig. 3.7. This difference is considered acceptable because flue gas fluctuations make accurate temperature measurements and predictions difficult. The boiler measurements are described in more detail in Chapter 3.7.

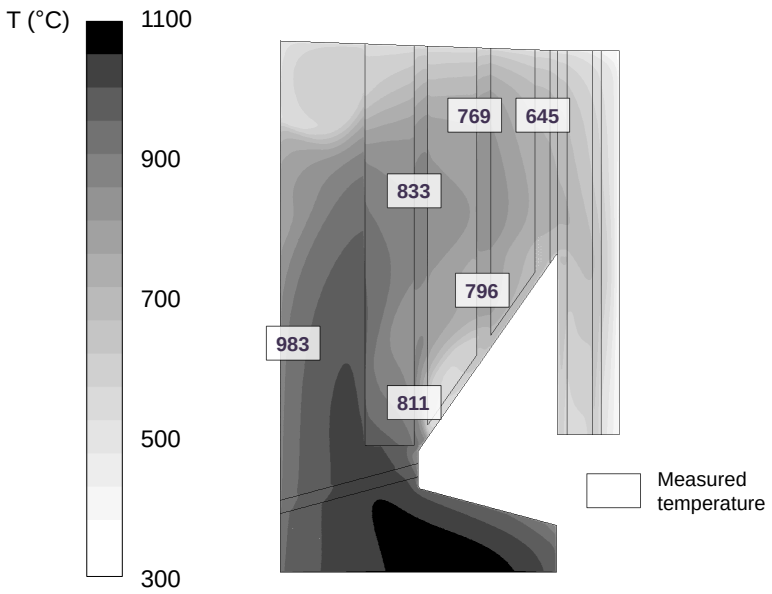

Fig. 3.7: Modeled and measured temperature values of Boiler B (Paper III).

Obtaining a realistic temperature distribution with the CFD model is important because temperature has a significant effect on the formation of fume particles and deposits. In addition to deposit thickness, other deposit properties affect temperature distribution. When modeling Boiler B, the deposits are assigned a constant thermal conductivity of 1.5 W/(K·m), which is within the conductivity range for ash deposits given by Zbogar et al. [87]. The deposit density is approximated as 1500 kg/m^3, which is roughly based on the values of Duhamel et al. [88]. Deposit density is difficult to determine because it changes due to sintering, which means the densification of porous solids [89].

3.6 Grid dependency

The quality of the computational grid is important when assessing the reliability of the CFD results. The discretization error is defined by Ferziger and Perić as

> "the difference between the exact solution of the conservation equations and the exact solution of the algebraic system of equations obtained by discretizing these equations" [47].

If the grid lacks sufficient density, the differential equations will be poorly discretized, and the discretization error may override all other uncertainties in the model [90]. It is often impossible to totally remove the discretization error because of computational restraints, but it is important to assess its significance.

The discretization error is minimized when the solution is converged to a grid-independent solution [47]. In Paper III, grid dependency for the superheater area of Boiler B was tested with respect to the temperature values at the center of the modeled area (Fig. 3.7). The flue gas temperatures were modeled with grids including 1.4 and 2.4 million cells in addition to the original grid of 800,000 cells. All grids consisted of structured hexahedral cells, and the results for the temperature values are shown in Table 3.5.

According to Table 3.5, the temperature values for points 1–5 are within 1.5% of each other, but for point 6, the difference is larger. This is due to the recirculation of the flue gas around this point, which makes the temperature fluctuate. On the basis of these results, it was concluded that the temperature distribution stays effectively the same on the yz-plane when increasing the number of the computational cells.

Fume particle formation is dependent on the temperature field (Fig. 3.7), whereas fume deposit formation depends on the temperature gradient in the x-

Table 3.5: Flue gas temperatures for the different superheater grids of Boiler B (Paper III). The measurement points are shown in Fig. 3.9 (p. 31).

Grid	Point 1	Point 2	Point 3	Point 4	Point 5	Point 6
$0.8 \cdot 10^6$	703	813	894	793	954	811
$1.4 \cdot 10^6$	701	807	885	793	941	840
$2.4 \cdot 10^6$	700	806	883	795	941	838

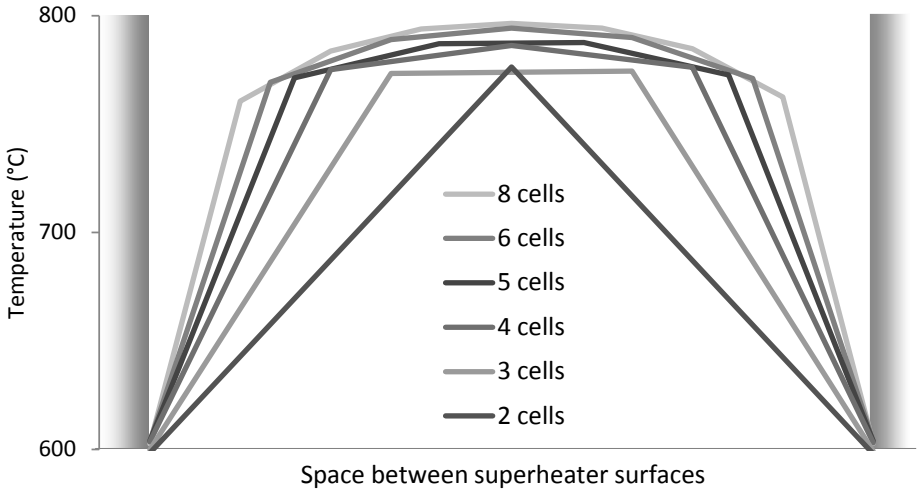

Fig. 3.8: Temperature distribution on the x-axis between two superheater platens in Boiler B simulated with varying number of cells.

Table 3.6: Average thermophoretic velocity on the primary superheater in Boiler B.

Cells on x-axis	2	3	4	5	6	8
$V_{th,ave}$(m/s)	0.072	0.056	0.054	0.052	0.051	0.051

direction, that is, the gradient between the flue gas and the superheater surfaces (see Eq. 3.7, p. 20). It is important, therefore, to refine the grid space between the superheater surfaces so that discretization error is minimized to an acceptable level in this direction. In this work, grid dependency in the x-direction was investigated on the primary superheater because here the thermophoretic velocities are high. Grid dependency was tested by increasing the number of computational cells in the space between the primary superheater platens. Figure 3.8 shows the node values of the temperature on the x-axis between the primary superheater platens, and Table 3.6 shows the average thermophoretic velocities on the primary superheater.

Figure 3.8 shows that the shape of the temperature distribution changes as the grid refinement on the x-axis increases. As a consequence, the temperature gradient near the wall becomes different for each grid, which has an effect on the thermophoretic velocity. However, the thermophoretic velocity does not increase with higher grid refinement, but instead, it decreases, as shown in Table 3.6. This surprising result occurs because the kinematic viscosity near the wall decreases with higher grid refinement, and this decreases the thermophoretic velocity. Table 3.6 shows that adequate grid refinement would be achieved with 6 cells on the x-axis between the primary superheater platens, but the simulations were conducted with 4 cells because the total number of computational cells had to

be limited. The resulting error is estimated to be 6%, which is acceptable when the purpose is to simulate the effect of operational changes in the boiler, and absolute values for the thermophoretic velocity are not significant.

Refining the grid between the primary superheater platens also affects the simulation results for the direct condensation of vapors but not to a significant degree when the refinement is 4 cells or more. With all the computational grids tested, NaCl is always the only compound that shows significant direct vapor condensation on the heat transfer surfaces.

3.7 Boiler measurements for partial model validation

Measurements were conducted in Boiler B, which is a 3,400 t_{ds}/d boiler running at almost full load and burning black liquor with 79.3% dry solids content. The composition of the black liquor burned in this boiler is presented in Table 3.3 (p. 23). Measurements were conducted in the superheater area of the boiler through measurement ports, the locations of which are shown in Fig. 3.9. The superheaters of Boiler B are presented in Fig. 3.5 (p. 25).

The flue gas temperatures were measured with a shielded K-type thermocouple, which was inserted horizontally about 1 m deep into the boiler for approximately 6 minutes. The averages of 2–3 measurements were used. In order to determine the accuracy of the thermocouple measurements, suction pyrometer measurements were performed at two locations. Since the results obtained were similar, only results obtained with the thermocouple were used. The results of the temperature measurements are presented in Fig. 3.7 (p. 27).

The fine particle measurements were conducted with a similar method to that of Aho et al. [91]. Fine fume particles were sampled using low pressure impactors, which divided the particles into size fractions. The impactor samples were later analyzed to obtain the particle composition. Additionally, the fly ash composition was analyzed immediately before the ESP. Before the impactor sampling, cyclones with 10 µm cut-off diameters removed large particles from sampling. The flue gases were diluted before entering the impactors in order to prevent condensation of the gaseous compounds in the measurement equipment. However, it appears that the gaseous alkali chlorides condensed in the measurement process despite the dilution. As a consequence, the gaseous and condensed alkali chlorides could not be distinguished from each other. According to Deuerling et al. [92], it is generally impossible to avoid the influence of all the potential factors on aerosol sampling.

Deposit samples were taken from measurement ports 2, 3, and 5. The samples were taken with deposit probes, which were water-cooled to temperatures corresponding roughly to the superheater tube temperatures (450–480 °C). The probes were kept in the furnace for one hour because the aim was to obtain a steady-state thickness for the deposits. However, it is uncertain whether the steady-state thickness was obtained, since the analyzed deposit compositions showed very high variation, especially with regard to chlorine content. After sampling, the com-

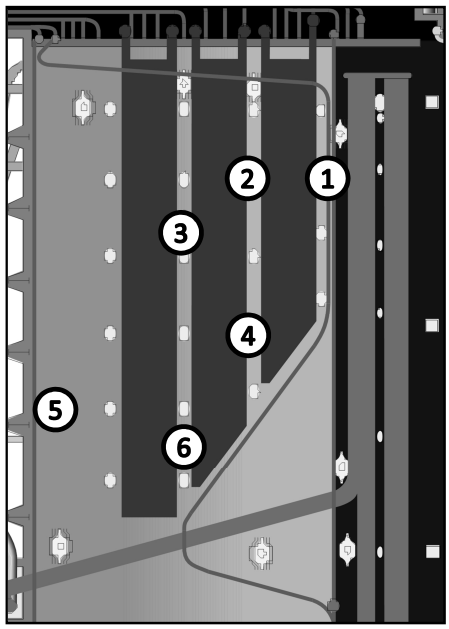

Fig. 3.9: Measurement locations in Boiler B (Paper III).

position of the deposit on the leeward side of the probe was analyzed because it contained mostly fume particles. The deposit on the windward side, by comparison, consisted mostly of carryover particles, which lie outside the focus of this study.

Chapter 4

Results and discussion

4.1 Furnace modeling

In Paper I, the furnace of Boiler A was simulated with the aim of testing and developing the modeling principle. The objective was to ensure that the predicted particle mass distribution is actually dependent on the temperature distribution, and that the results given by the model are comparable with the values quoted in the literature. In Paper I, the formation of particle nuclei from the gaseous Na_2SO_4 was modeled, but the formation of sodium and potassium carbonate was excluded for simplification.

The following figures are examples of the modeling results obtained for Boiler A. Figure 4.1 shows the temperature distribution in the boiler furnace and Fig. 4.2 the distribution of the gaseous KCl. Figure 4.3 shows the distribution of the fume particle mass concentration.

Figures 4.1 and 4.2 show that the distribution of the gaseous KCl is almost proportional to the temperature distribution. According to the chemical equilibrium calculations, KCl becomes partly sulfated to K_2SO_4 when the temperature decreases. Moreover, the remaining gaseous KCl is supersaturated in the low temperature areas and condenses on the fume particles. It is noteworthy that only a fraction of the gaseous KCl disappears in the boiler furnace, because the temperature remains high at the furnace outlet. Sodium chloride is expected to behave like potassium chloride, while most of the alkali sulfates should condense already in the furnace since the equilibrium vapor pressures of alkali sulfates are much lower than those of alkali chlorides (Fig. 3.2, p. 17). In addition to temperature and the vapor pressure function, the location of supersaturation also depends on the partial pressure, or the mole fraction, of the condensing compound (Eq. 3.6, p. 17).

Figure 4.3 shows that as the flue gases cool, the alkali metal compounds start to condense on particles, increasing the fume particle mass concentration. However, the increase seems to be exaggerated in the modeling results as the scale in the figure is lognormal and the maximum particle concentration is 100 g/Nm^3. It seems that the result in Paper I had not fully converged with respect to

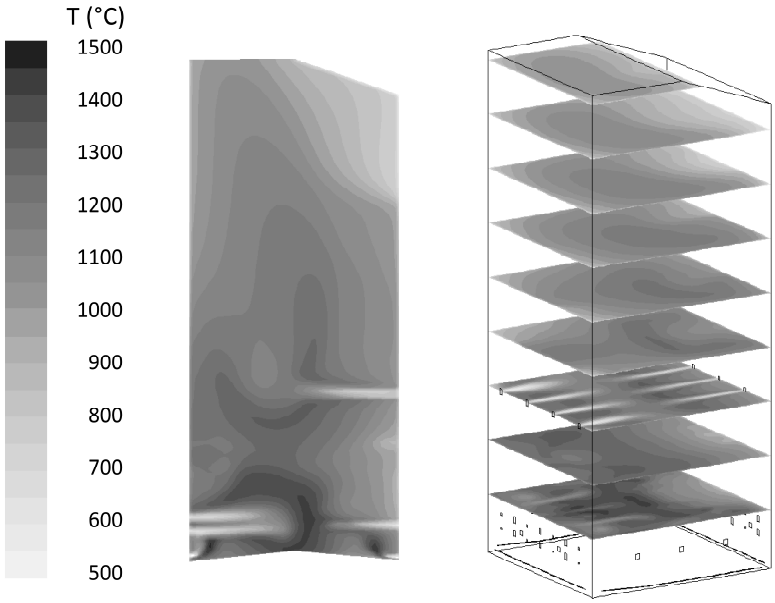

Fig. 4.1: Temperature distribution for Boiler A (Paper I).

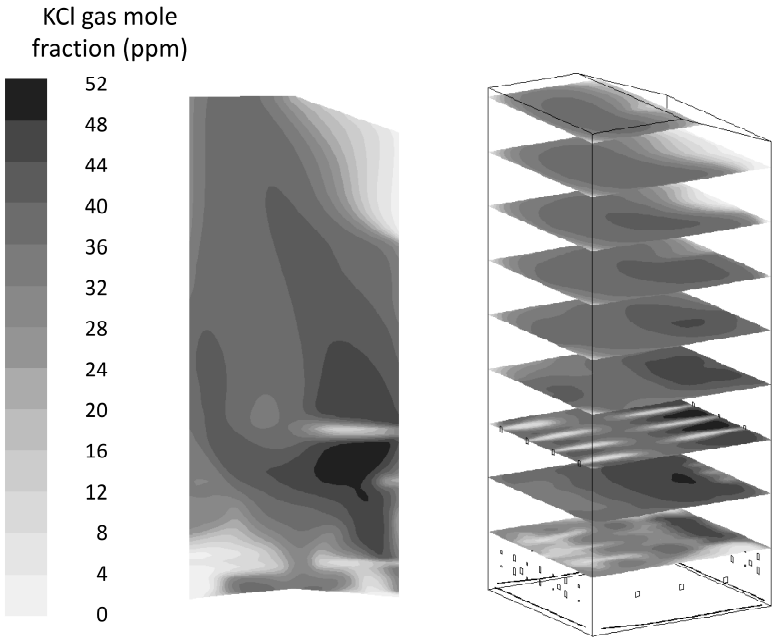

Fig. 4.2: Distribution of gaseous KCl for Boiler A (Paper I).

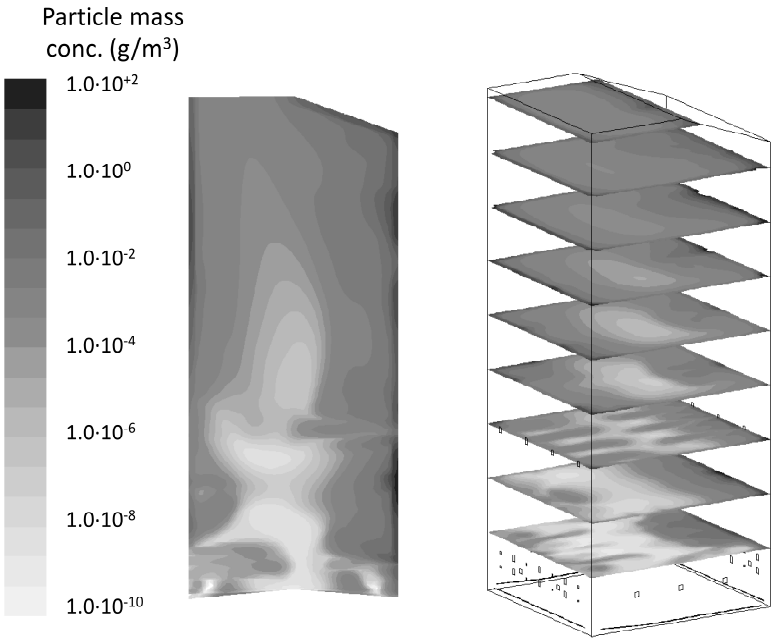

Fig. 4.3: Fume particle mass concentration for Boiler A (Paper I).

coagulation and particle transport, because coagulation should make the particle mass concentration more evenly distributed [2, 70]. Because of this incomplete convergence, the results for the geometric mean particle diameter and the particle number distribution are not presented here. However, the average fume particle concentration given by the model is approximately 6 g/Nm^3, which seems realistic compared to an average value of slightly over 10 g/Nm^3 given by Mikkanen et al. [31] for particles below 3 μm in diameter. The difference of the modeling result from this value may be due to the chosen release factors (Table 3.1, p. 12), the incomplete convergence of the modeling results, or the fact that not all alkali metal compounds condensed in the boiler furnace.

The modeling of Boiler A was developed in Paper II to include also the formation of alkali carbonates, and the modeling results were compared with the measurement results of Tavares and Tran [93]. These measurements were conducted in a recovery boiler in North America. In the measurements, a fume deposition probe, which was protected from carryover particles by encapsulation, was used to investigate the composition of fume at different locations in the boiler. Unfortunately, the operation parameters of this boiler are not available, so the same boiler could not be modeled. However, the comparison of the modeling results for Boiler A and these measurement results can give information on how realistically the model predicts the conditions in a recovery boiler.

Figure 4.4 shows the comparison of the modeling results for the flue gas composition in the lower furnace with the deposit composition obtained by the measurements of Tavares and Tran [93] in another boiler. The results are shown for

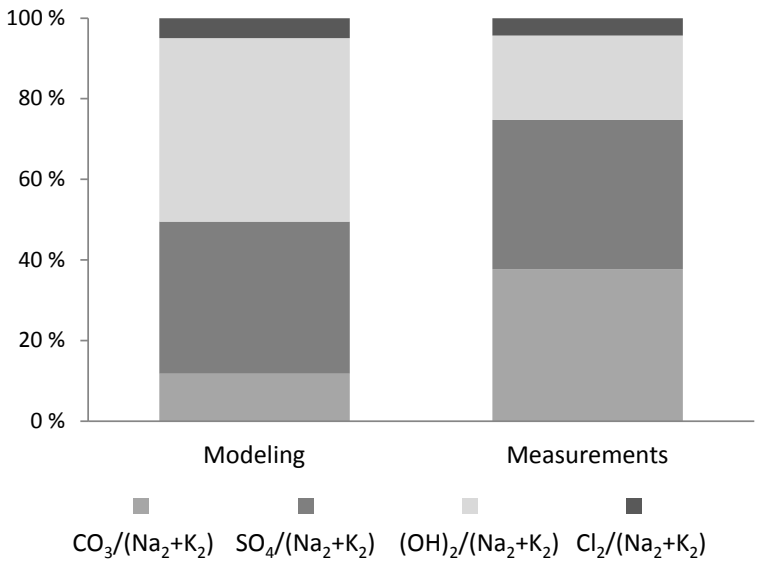

Fig. 4.4: Comparison of lower furnace modeling results in Boiler A to the measurements of [93] (Paper II).

the anion (CO_3, SO_4, $(OH)_2$, and Cl_2) composition divided by the total amount of the cations (Na_2 and K_2).

As stated in Chapter 3.2, the model assumes oxidizing conditions in the equilibrium calculations, which may have affected the simulation results in the lower furnace. It is possible that the measurement conditions around the deposition probe, which was located next to a black liquor gun port, were reducing. This may have caused the difference in the carbonate and hydroxide mass fractions between the modeling and the measurements results in Fig. 4.4. Another possible reason for the difference is that the furnace deposit probe had to be cooled to protect it from corrosion, and this may have induced some chemical reactions inside the cooled probe. The model cannot predict these reactions in the condensed phase because it assumes that the equilibrium reactions of the alkali metal compounds only occur in the gaseous phase.

In contrast to the results for carbonates and hydroxides, the modeling results for sulfates and chlorides are similar to the measurement results. This indicates that the model can realistically predict the sulfation of alkali chlorides using the equilibrium assumption. In conclusion, however, the developed model cannot accurately predict the alkali metal chemistry in the lower furnace due to the partly reducing atmosphere there.

4.2 Superheater modeling for Boiler A

Figure 4.5 shows the modeled temperature distribution for the superheater area of Boiler A. The temperature is modeled in the middle of the boiler. A recirculation

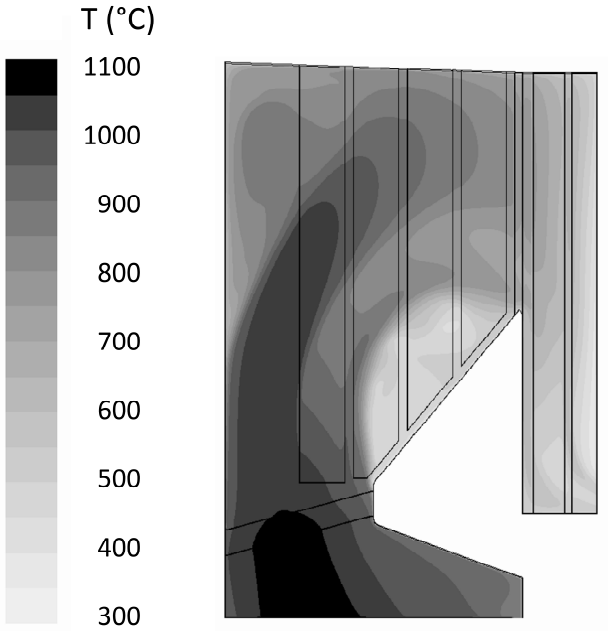

Fig. 4.5: Modeled temperature distribution between two middle superheater platens in Boiler A (Paper II).

area can be identified just above the bullnose in Fig. 4.5. Recirculation areas have been identified in real boilers as well, but they are undesirable from the heat transfer point of view. In a recirculation area, the direction of heat transfer may be reversed, and the superheated steam may release heat to the flue gases [94].

The comparison of the modeling results in Boiler A and the measurement results of Tavares and Tran [93] in a different boiler was extended to include the superheater area in Paper II. In this paper, the measured fume deposit composition was compared with the modeled fume particle composition because deposition had not yet been included in the model. Figure 4.6 (upper part) shows the modeled fume particle composition for nine different points (1 to 9) from the beginning of the superheater area until the boiler bank at approximately the same locations as those used for the field measurements. The same figure (lower part) shows the measured composition of the fume deposits collected at eight different points (labeled B to I) and also the precipitator dust (ESP ash) [93]. Although the modeling and measurement results are not obtained from the same boiler, they both show how the fume composition develops through the superheater area. The measured dust composition is compared to the modeled composition for fume after the point at the boiler bank where the computational grid ends because the boiler bank deposit should have a similar composition to the precipitator dust [95]. According to equilibrium calculations, all the alkali metal compounds should have condensed at the boiler bank, and the fume composition is not expected to change after that.

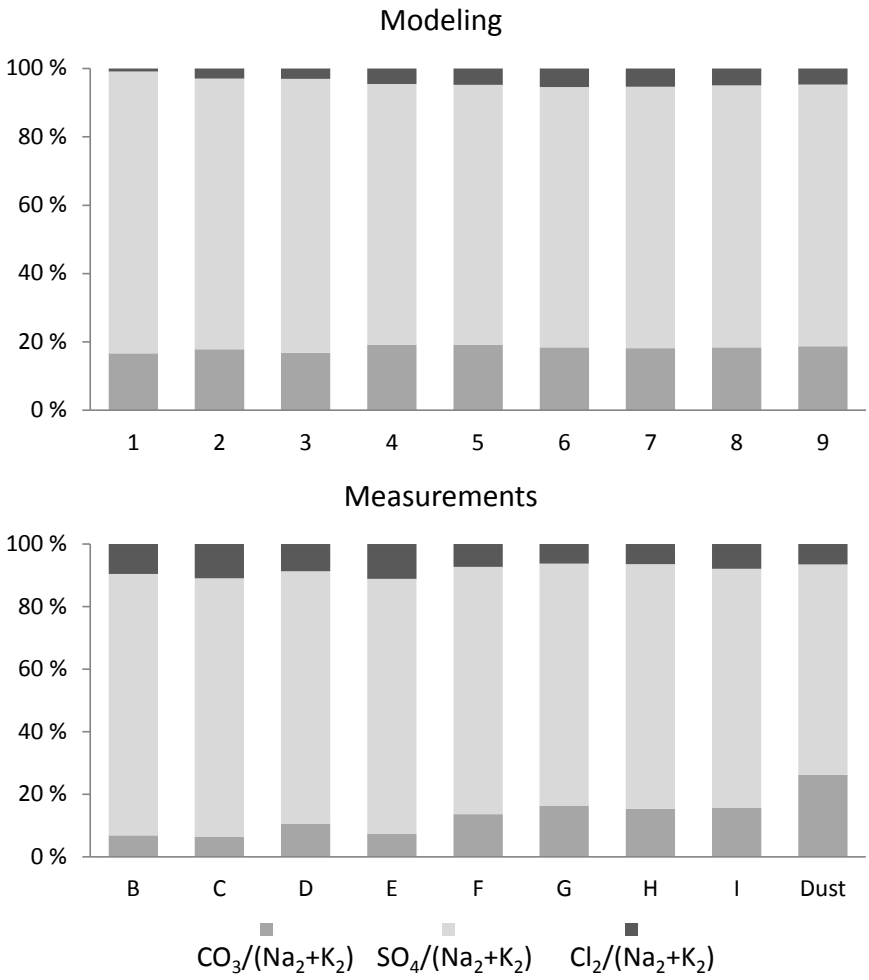

Fig. 4.6: Comparison of superheater modeling results in Boiler A to the measurements of [93] (Paper II).

The correspondence between the modeled fume particle and the measured fume deposit composition is relatively good because the superheater conditions in the two boilers were similar. For the chlorine mass fraction, the modeling shows growth from 1 to 5% when moving downstream the flue gas flow. The growth ceases when all the gaseous alkali chlorides have condensed on the particles. The measurements, on the other hand, show a large variation in the chlorine fraction (6 to 11%), which indicates fluctuating conditions in the boiler or difficulties in measuring chlorine. The reason no growing trend is observed in the measured Cl content is most likely because the gaseous alkali chlorides have condensed on the measurement probe. The model, on the other hand, predicts that most alkali chlorides should still be in the gaseous phase in the hottest superheater locations. There might also have been more chlorine in the black liquor of the measured boiler than in the modeled boiler, but this is unknown.

There is also a discrepancy between the modeled and measured values for the carbonate ions. The model gives an almost constant carbonate content of 18%, whereas the measured values increase through the measurement points, reaching 25% in the precipitator dust. This increasing trend is difficult to explain because alkali carbonates should form and condense in relatively high temperatures ($>$ 800 °C), according to the equilibrium calculations conducted (Fig. 3.1, p. 13) and the measurement results obtained in this work (Table 4.1, p. 40). However, it is possible that under certain conditions, the formation of alkali carbonates is slower than that predicted by equilibrium calculations. This would explain the increasing trend observed in the presented [93] and earlier measurements by Tavares et al. [96]. On the other hand, the high carbonate content in the ESP ash could be explained by flow instabilities or the re-entrainment of superheater deposits due to sootblowing since such high content was not observed in the earlier measurements [96]. The model cannot capture these instabilities because the simulations are not time-dependent.

Another way to assess the reliability of the modeling results is to calculate enrichment factors for the non-process elements, chlorine and potassium. The enrichment factors are calculated by

$$\mathrm{EF_i} = \frac{\mathrm{i_{fume}} / \left(\mathrm{Na_{fume}} + \mathrm{K_{fume}}\right)}{\mathrm{i_{BL}} / \left(\mathrm{Na_{BL}} + \mathrm{K_{BL}}\right)}, \tag{4.1}$$

where Na and K are the molar fractions of sodium and potassium, respectively, and i can be replaced with the molar fraction of K or Cl. Typical enrichment factors in the recovery boiler fume are 1.5–3 for potassium, and closer to 3 for chlorine [20]. The values obtained for the fume particle composition at the end of the modeled superheater area are 1.3 for potassium and 2.5 for chlorine, which shows that the release factors used (Table 3.1, p. 12) were probably realistic.

In addition to the fume composition, the gaseous compounds can also be investigated. Figure 4.7 presents the modeled distributions of the gaseous SO_2 and gaseous KCl.

The results for the sulfur dioxide distribution in Fig. 4.7 show that SO_2 almost disappears from the flue gases in the superheater area. This is a result of the alkali sulfate formation according to reactions 2.1 and 2.2 (p. 7). In general, the sulfur

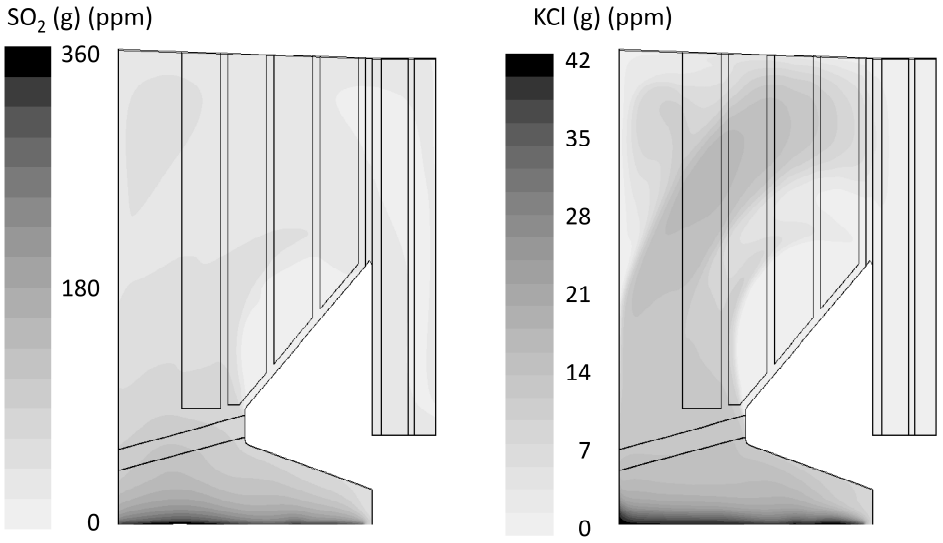

Fig. 4.7: Modeled distribution of gaseous SO_2 and gaseous KCl in the superheater area of Boiler B (Paper II).

dioxide emissions of kraft recovery boilers have decreased from several hundreds of ppm in the 1970s to practically zero in modern boilers [9]. Figure 4.7 also shows how the gaseous KCl disappears. At the beginning of the superheater area, the KCl concentration decreases rapidly, mainly because of sulfation to K_2SO_4. In contrast, the later decrease is a result of condensation on the fume particles, which occurs when the temperature cools even more. The molar concentration of gaseous KCl, which is 0 to 36 ppm in the superheater area, seems to be in the same range as the modeling results of Jokiniemi et al. [2] and Wessel et al. [45].

Along with the fume composition comparison in Fig. 4.6, the distribution of the gaseous compounds in Fig. 4.7 confirms that the model gives realistic results, despite the minor differences between the modeled and measured fume composition. The results for the particle mass concentration are not presented here, because the results in Paper II had not fully converged, and the results showed that there were pockets of very high fume mass concentrations. The slow convergence of the coagulation and particle transport processes became evident only later. Nevertheless, even the incomplete results in Paper II indicate that the fume particle mass starts to form already at the beginning of the superheater area with the condensation of alkali sulfates and carbonates. This is in contrast to the measurement results of Tavares and Tran [93], which show a sudden increase in the particle mass at a location near the boiler bank inlet, where the flue gas temperature was 550–650 °C. This temperature is significantly below the melting temperature of KCl, 770–775 °C [93, 97], which is the lowest melting temperature of the alkali compounds. The onset of particle formation at such low temperatures might be possible if no particle nuclei existed in the boiler, since nucleation requires high supersaturation ratios (see Chapter 3.3). However, it is assumed that inert particle nuclei exist in the boiler, which enables particle growth by

condensation already at the beginning of the superheater area. Mikkanen [9], too, reports that significant amounts of fume particle mass appear before the gases reach the boiler bank.

4.3 Superheater modeling for Boiler B

Another conclusion from Paper II was that the developed model should be tested against fume measurements conducted in a boiler, which could also be modeled. This goal was achieved in Paper III, which presents the measurement and modeling results for Boiler B. In this paper, the fume deposit formation was included in the model. For Boiler B, the operation variables and the boiler geometry were known, so it was possible to model the same boiler. The furnace modeling results for Boiler B are not presented here, because the furnace model was only used to generate input conditions for the superheater area, which was the focus of this work.

Table 4.1 shows the comparison between the measured and modeled fine fume particles in Boiler B. The measured particles are captured with low-pressure impactors, as explained in Chapter 3.7. The measurement points 2, 3, and 5 are shown in Fig. 3.9 (p. 31). In the last column, the measured composition of the ESP ash is compared with the modeled fume particle composition at the location where the computational grid ends at the boiler bank (after bb).

The agreement between the modeled and measured fume particle composition is relatively good, as most of the modeling results fall within 15% of the measurements. This supports the release factor approximations for the ash-forming elements (Table 3.1, p. 12) in this particular case. There are small differences in the potassium, carbonate, and sulfate contents, but these may be due to minor inaccuracies in the release factors used. However, there is significant disagreement with regard to the chlorine content: the measurements show an average chlorine content of about 0.4%, whereas the modeling shows an increase from 0.1 to 0.3%. It seems that in the measurements, the impactors also captured the gaseous alkali chlorides, which later condensed despite an attempt to prevent this by strongly diluting the flue gas. The modeling, on the other hand, predicts that because of their high equilibrium vapor pressures, some alkali chlorides remain

Table 4.1: Composition in wt-% of the modeled and measured fine fume particles (Paper III). The measurement points are shown in Fig. 3.9 (p. 31).

Grid	Point 5		Point 3		Point 2		ESP ash/after bb	
	Meas.	Model	Meas.	Model	Meas.	Model	Meas.	Model
Na	32.0	33.6	32.8	33.4	33.5	33.5	34.0	33.5
K	2.0	2.2	2.0	2.2	2.0	2.2	1.8	2.2
CO_3	13.3	14.2	12.0	13.5	11.0	14.0	12.0	13.5
SO_4	52.3	50.0	52.8	50.7	53.0	50.1	51.7	50.4
Cl	0.5	0.1	0.4	0.1	0.4	0.2	0.3	0.3

Table 4.2: Composition in wt-% of the modeled and measured fume deposits (Paper III). The measurement points are shown in Fig. 3.9 (p. 31).

Grid	Point 5/Screen		Point 3/Sec. sh		Point 2/Tert. sh		Prim. sh	Bb
	Meas.	Model	Meas.	Model	Meas.	Model	Model	Model
Na	30.3	34.3	30.7	34.3	30.9	34.4	34.5	34.4
K	2.2	2.3	2.4	2.3	1.9	2.3	2.3	2.3
O	47.8	45.9	48.8	45.8	47.6	45.8	45.8	45.7
S	19.2	17.5	17.0	17.4	19.6	17.3	17.2	17.3
Cl	0.5	0.0	1.1	0.1	0.0	0.2	0.3	0.3

in the gaseous form at measurement points 2, 3, and 5. At the final point of comparison (ESP ash/after bb), the measured and modeled chlorine contents are similar, since at this location, the model predicts that all alkali chlorides have condensed on the particles.

The modeled average size of the fume particles is approximately 0.4 μm, which corresponds to the measurements of Mikkanen et al. [31]. However, the fume particle composition is not shown separately for the different particle size fractions. This is because the presented model assumes that the fume particles consists of only one particle mode, and the dependence of particle composition on particle size was not simulated. However, according to the measurements, the particle composition was the same for all particle sizes below the impactor cut-off diameter of 10 μm. The same result has been obtained by the simulations of Eskola et al. [32], though opposing views have also been presented. It is possible that alkali chlorides sometimes enrich into smaller particles because they are in the vapor phase prior to sampling, and nucleate in the sampling process [51].

The comparison between the measured and modeled fume deposits is shown in Table 4.2. In this case, the measured deposits are obtained by deposition probes at points 2, 3, and 5, whereas the modeled average deposit compositions are presented for the nearby three superheater surfaces: the screen, the secondary superheater, and the tertiary superheater. The modeled deposit compositions for the primary superheater and the boiler bank are also shown, but there are no measurement results available for these locations. It is important to note that the modeled compositions are the surface-averaged instantaneous compositions of the fume deposits that form on the superheaters in the given boundary conditions.

Again, the measured and modeled values are within 15% of each other, except for chlorine. The measurement results for chlorine are very uncertain, varying from 0 to 1.1%. A possible reason for this is that the abnormally low chlorine content in the black liquor might have made its detection difficult. In contrast to the measurement results, the modeling results show an increase in the chlorine content from 0 to 0.3%, resembling the development of the fume particle composition. This is not surprising, since the deposition of fume particles on the superheater surfaces is the most significant fume deposit formation mechanism, according to the modeling results.

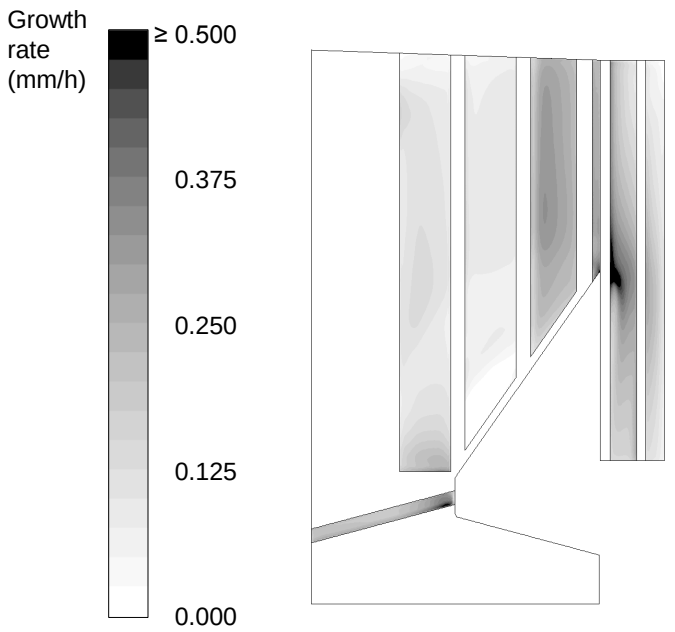

Fig. 4.8: Modeled distribution of the instantaneous fume deposit growth rate on the superheaters for Boiler B (Paper III).

In addition to the deposit composition, the results for the fume deposit growth rate can be examined. Figure 4.8 shows the instantaneous fume deposit growth rate on the superheater surfaces. The presented growth rate is instantaneous because the modeling is not dependent on time, and the deposit growth is not simulated. Instead, the instantaneous growth rate depends on the given boundary conditions (Table 3.4, p. 27). In reality, the deposit thickness is constantly changing, which would also change the deposit growth rate. In order to determine how much the changing boundary conditions affect the growth rate, the model's sensitivity to the given boundary conditions, such as the deposit thickness, is discussed in Chapter 4.4.

The results in Fig. 4.8 show that the deposits grow fastest on the primary superheater and the boiler bank. According to the model, the alkali sulfates and carbonates condense on the particles already at the beginning of the superheater area, so the location of particle growth does not cause the high deposition rate on these surfaces. Instead, the deposition rate is high in the primary superheater and the boiler bank because there the superheater tubes are spaced closer together than in the earlier superheaters, which increases the temperature gradients. Thermophoresis is directly dependent on the temperature gradient (Eq. 3.7, p. 20), and this seems to be the main fume deposit formation mechanism.

Locally, the highest fume deposit growth rate is where the flue gas flow turns downwards at the boiler bank, reaching maximum values of slightly below 0.9 mm/h. At this location, the thermophoretic velocity increases significantly due to the high turbulent kinetic energy and more specifically, the high kinematic vis-

cosity of the flue gas. The average kinematic viscosity near the surface increases from around 0.005 m^2/s to about 0.007 m^2/s when moving from the primary superheater to the boiler bank. However, it reaches a maximum value of 0.05 m^2/s at the flue gas turning point, leading to faster fume deposit growth. The instantaneous deposit growth rate also seems high on the screen, but the result is misleading. In reality, the deposit growth on the screen is limited because the deposit surface temperature exceeds T_{70}, the radical deformation temperature [77]. Above this temperature, the deposit contains so much liquid that it flows away, and the deposit growth is restricted. The value of T_{70} depends on the deposit composition. For the boiler in question, this is approximately 820 °C when calculated for the fume deposit composition.

The modeled instantaneous average growth rate is slightly below 0.1 mm/h for the tertiary superheater and below 0.3 mm/h for the primary superheater. Unfortunately, the fume deposit growth rate was not measured in Boiler B. However, the modeling results can be compared with several results in the literature. For example, the measurements of Mikkanen [9] gave a growth rate of 0 to 0.2 mm/h for the leeward side deposits in a kraft recovery boiler, and the location of these measurements corresponded roughly to the space between the secondary and the tertiary superheater in the modeled boiler. The growth rates simulated in this work are also in the same range as the modeling results of Wessel and Baxter [8], although their results do not distinguish between the deposition of fume, ISP, and carryover particles.

Furthermore, the modeled fume deposit growth rate is similar to the value of Pyykönen and Jokiniemi [28], which is about 7 $g/(m^2 min)$, corresponding to roughly 0.3 mm/h if the density assumption of 1500 kg/m^3 is used. In their work, the fume deposit growth was modeled with a grid that was much more refined than the grid in this case, because their grid covered only a small area at the front of the first superheater tube at the entrance to the superheater section. In contrast, the fume deposit growth rate obtained in this work differs markedly from the results of Eskola et al. [32], where the thermophoretic velocity is approximately 10 times lower than the value obtained by the presented model. It is probable that a significant difference in the simulated temperature gradients causes this discrepancy.

As stated above, deposition by thermophoresis seems to be the main fume deposit formation mechanism for the superheaters and the boiler bank of the recovery boiler. The same conclusion is drawn by Jokiniemi et al. [2] based on simulations, and by Cameron and Goerg-Wood based on experiments [78]. However, this view is contradicted by the experiments of Sinquefield et al. [79], where the rate of fume deposition stayed almost constant when the driving force for thermophoresis decreased. This would imply that fume deposits by some other mechanism than thermophoresis. On the other hand, the observation might be due to the fact that the calculated driving force was based on ΔT (difference) and not on ∇T (gradient), which is found in the equation for thermophoresis (Eq. 3.7, p. 20). Nevertheless, this observation prompted the authors to develop an alternative and more accurate equation for fume deposition [98], but it seems that their work is unfinished.

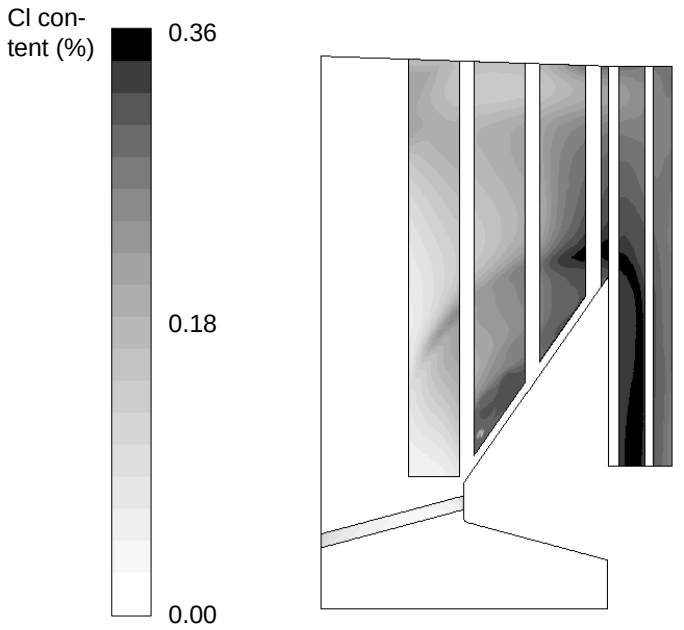

Fig. 4.9: Modeled chlorine content of the fume deposits for Boiler B (Paper III).

In addition to thermophoresis, deposition by diffusion was also modeled in this work, but it accounted only for less than 0.01% of the total fume deposit formation. This was expected because diffusion is the most important deposition mechanism only for particles smaller than 0.1 μm [34], and the simulated particles are approximately 0.4 μm in size. The role of diffusion was also found to be negligible in a biomass-fired grate boiler by Zhou et al. [99].

The role of direct vapor condensation on heat transfer surfaces is also insignificant almost everywhere in the current boiler simulation. The only compound that seems to condense directly is NaCl, of which as much as 2% can form deposits in this way at the lower primary superheater. Direct vapor condensation on the heat transfer surfaces occurs when condensation on particles is unable to prevent significant supersaturation close to a surface [28]. It can be argued that the initial amount of the particle nuclei could affect the amount of alkali vapors that condense directly. However, tests show that even 100-fold changes in the initial amount of the particle nuclei do not significantly affect direct vapor condensation. On the other hand, larger changes in the amount of the nuclei are not possible because they would result in an unrealistic size distribution for the fume particles.

As stated above, the presence of chlorine in the superheater deposits can expose the superheater tubes to corrosion. Because of this, the chlorine content of the deposits is an important parameter, and for Boiler B, it is presented in Fig. 4.9. The figure shows the chlorine content of the fume deposit forming in the given boundary conditions. The chlorine content in the underlying deposit may be different, but this issue is further investigated in the next chapter.

The chlorine content of the fume deposits increases when the flue gases cool because the alkali chloride vapors become supersaturated and condense on the fume particles, which subsequently deposit. Additionally, a small fraction of NaCl becomes so highly supersaturated at the primary superheater that it condenses directly on the surface. However, the chlorine content is not only dependent on the temperature of the flue gas. In the coldest areas of the boiler bank, the Cl content is not as high as expected, because the alkali chlorides seem to have reacted to form alkali sulfates to a large extent. Overall, there are differences between the chlorine contents of the deposits on the different heat transfer surfaces in Fig. 4.9, but the differences are relatively small. However, for a boiler burning black liquor with a higher chlorine content, the differences could be more pronounced. This is in contrast to the findings of Pyykönen and Jokiniemi [28], who claim that no large variations in the deposit chlorine contents should be expected as a result of different fume deposition mechanisms in the various areas of the superheaters. As a consequence, the next section investigates whether changes in the boiler boundary conditions affect the deposit Cl content.

4.4 Model sensitivity analysis

As explained earlier, this model assumes that deposits of constant thicknesses always exist on the superheater surfaces, and that new deposits form on top of these initial deposits. The deposit thickness on each superheater is an important boundary condition because the thickness does not change in the steady-state calculations. In the simulations presented in Chapter 4.3, the initial deposit thicknesses were chosen so that the modeled flue gas temperatures closely correspond to the measured temperature values. In practice, however, the deposit thicknesses vary with time due to deposit growth, sootblowing, and other erosion mechanisms. This section evaluates the model's sensitivity to the initial deposit thickness on the primary superheater. The primary superheater was chosen for the investigation because, according to the modeling results for Boiler B, it is the location of the highest fume deposition rate. Table 4.3 shows the different deposition thicknesses used in the sensitivity analysis, where the deposit thickness for the baseline simulation is the same as in Chapter 4.3.

The deposit thickness on a superheater affects the heat transfer from the flue gases to that superheater, which, in turn, affects the deposit surface temperature and the flue gas temperature in the vicinity of the superheater. Both of these are parameters in the equations for thermophoresis (Eq. 3.7, p. 20) and for direct vapor condensation (Eq. 3.11, p. 22). A change in the deposit thickness on a

Table 4.3: Initial deposit thicknesses on the primary superheater in the different simulations.

Case	A (baseline)	B	C
Deposit thickness (mm)	34	27	20

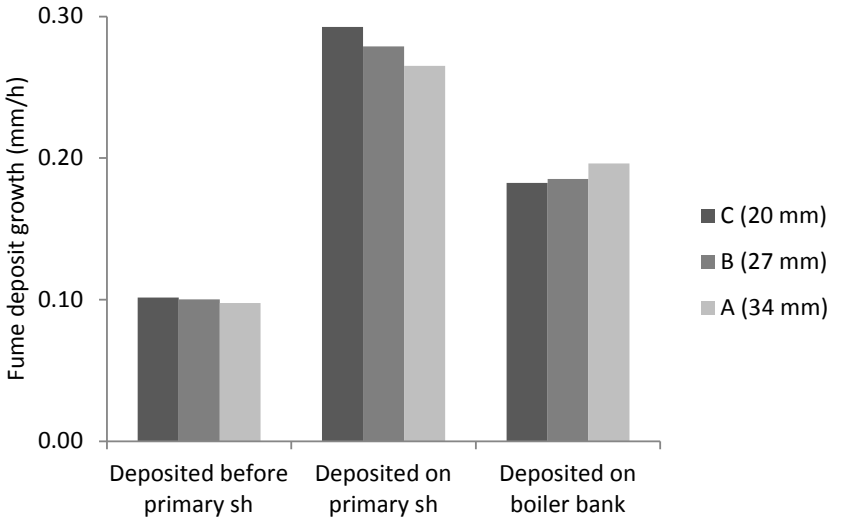

Fig. 4.10: Modeled average instantaneous fume deposit growth rates (mm/h) on the different superheater surfaces when the initial deposit thickness on the primary superheater was changed (Paper IV).

superheater also changes the width of the flue gas channel, which affects the value of kinematic viscosity, another parameter in the equation for thermophoresis.

Figure 4.10 shows the modeled average fume deposit growth rate on different superheaters when the initial deposit thickness on the primary superheater is changed. The columns are in the order of increasing initial deposit thickness, simulating deposit growth. In all the simulated cases, the deposit growth rate is distributed in a similar way to Fig. 4.8 (p. 42).

As can be seen in Fig. 4.10, the modeled fume deposit growth rate on the primary superheater slowly decreases when the initial deposit thickness on that superheater increases. This occurs because the increasing deposit thickness acts as an insulator and decreases the rate of heat transfer. This, in turn, increases the deposit surface temperature and lowers the temperature gradient between the flue gas and the deposit surface, which together lower the thermophoretic velocity (see Eq. 3.7, p. 20). This observation means that the fume deposit growth is a self-limiting process, at least when it is governed by thermophoresis.

When the initial deposit thickness on the primary superheater is changed, there is no significant effect at the modeled deposit growth rate before the primary superheater. However, the fume deposit growth rate on the boiler bank seems to increase. This effect can be explained by the slightly higher flue gas temperatures entering the boiler bank, because the flue gases cool less at the primary superheater. The higher gas temperatures at the boiler bank somewhat increase the temperature gradient and the kinematic viscosity, which both increase deposition by thermophoresis. Earlier, it has been known that fouling of one superheater may increase the deposition of carryover particles on the surfaces downstream [33], but it seems that this may be true for fume deposition as well.

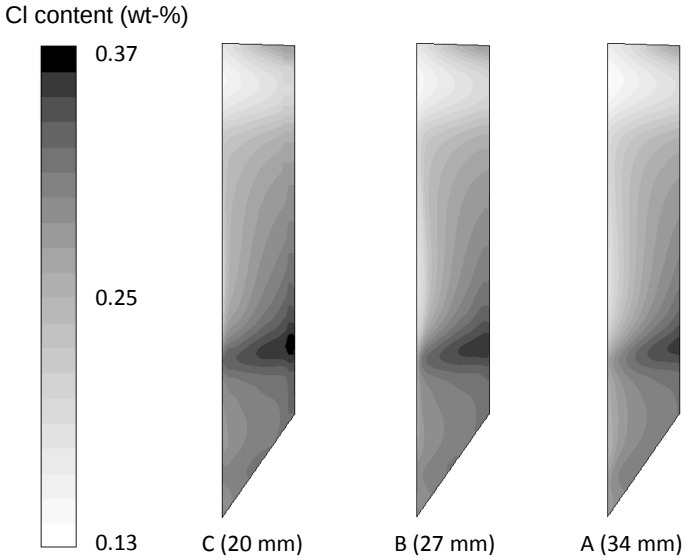

Fig. 4.11: Modeled instantaneous Cl content (wt-%) of fume depositing on the primary superheater when the initial deposit thickness on the primary superheater is changed (Paper IV).

In addition to the fume deposit growth rate, the change in the initial deposit thickness may also affect the composition of the forming fume deposit. Figure 4.11 shows how changing the deposit thickness on the primary superheater affects the modeled chlorine content of the fume deposit that forms on that superheater. Only the change in the chlorine content is shown because the alkali chloride condensation occurs at the temperatures that changed between the different simulated cases. In contrast, the alkali sulfates and carbonates condense already in the higher temperatures upstream from the primary superheater.

Figure 4.11 shows that when the initial deposit thickness on the primary superheater increases, there is a small decrease in the modeled chlorine content in the fume deposit forming on that superheater. An explanation for the change in the chlorine content can be found when the different chlorine deposition mechanisms are investigated. Figures 4.12 and 4.13 show the amount of chlorine that deposits through thermophoresis and through the direct condensation of vapors in the different simulated cases. The growth rate is shown for the chloride ions, although in reality, the condensing and depositing compounds are NaCl and KCl.

When the initial deposit thickness on the primary superheater increases, the amount of chlorine depositing through thermophoresis decreases slightly, as shown by Fig. 4.12. There are two explanations for this. First, the amount of chlorine that condenses on the particles is lower in the slightly higher flue gas temperatures, and second, the lower temperature gradient between the flue gas and the deposit surface decreases the rate of fume deposition by thermophoresis, as explained earlier. In contrast to deposition by thermophoresis, the amount of chlorine that directly condenses on the deposit surface (Fig. 4.13) decreases sig-

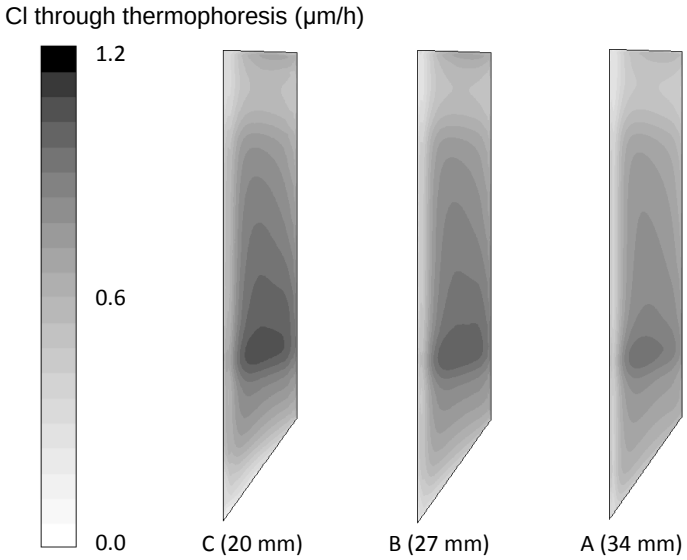

Fig. 4.12: Modeled instantaneous rate of chlorine deposition through thermophoresis (µm/h) on the primary superheater when the initial deposit thickness on the primary superheater is changed (Paper IV).

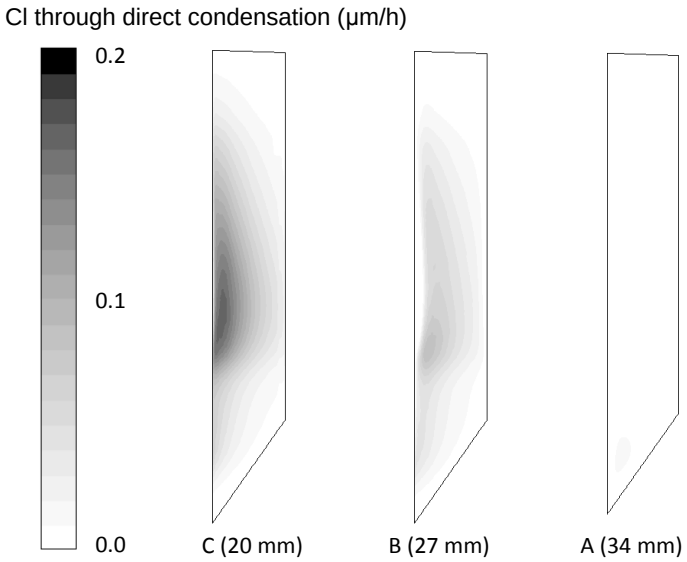

Fig. 4.13: Modeled instantaneous rate of chlorine deposition through direct vapor condensation (µm/h) on the primary superheater when the initial deposit thickness on the primary superheater is changed (Paper IV).

Table 4.4: Changes in the flue gas inlet temperature in the different simulations.

Case	D	A (baseline)	E
Temperature change (°C)	-50	0	+50

nificantly when the initial deposit thickness on the primary superheater increases. This occurs because the higher deposit surface temperatures (cases A and B) decrease the supersaturation of the alkali chlorides near the deposit surface, which makes most of the alkali chlorides condense on the fume particles first, and not directly on the surfaces.

This result is in contrast to the modeling results of Pyykönen and Jokiniemi, which show that the direct vapor condensation of NaCl increases when the deposit thickness increases [28]. However, the modeling results of Zhou et al. [99] are in agreement with the results in this thesis because they state that both the deposition due to thermophoresis and the direct vapor condensation decrease when the deposit thickness increases. The simulations presented here show that when the deposit is thin (case C), the amount of chlorine that directly condenses on the surface is notable (Fig. 4.13), but still much lower than the amount that deposits via thermophoresis (Fig. 4.12). The relative importance of direct vapor condensation might increase if the modeled boiler was burning black liquor with a higher chlorine content, but this has not been tested yet.

The results in Figs. 4.11-4.13 indicate that, in general, more chlorine can be found in the deposit layers closer to the superheater tube surfaces. In the case when the superheater surface would be completely free of deposits, the amount of depositing chlorine could be significantly high and detrimental in terms of corrosion. Another explanation for the higher chlorine content near the boiler tubes was recently offered by Lindberg et al. [100]. They state that in the hotter parts of porous salt deposits, the alkali chlorides may become vaporized and transported to the colder parts of the deposits, where they condense again. However, it is possible that the recovery boiler deposits are not porous enough to allow this transportation.

The second part of the sensitivity analysis investigates the effect of the flue gas temperature on fume deposition. In practice, the temperature of the flue gas entering the superheater area can change due to variation in the boiler operation, such as the boiler load or liquor heating value. Furthermore, the temperature of the flue gas varies in the different cross sections of the superheater area (see Fig. 3.5, p. 25), and therefore it is important to investigate the model's sensitivity to the flue gas temperature. Table 4.4 shows how the flue gas temperature entering the superheater area is changed in the different simulations.

It is noteworthy, that the release factors of the elements (Table 3.1, p. 12) are kept constant in the different simulations, although it is known that the release of Na, K, and Cl increases and the release of S decreases when the lower furnace temperature increases. However, the magnitudes of the changes are not known. Also, the boundary conditions of the superheater surfaces (tube surface temperature and deposit thickness) remain unaltered in the simulations. Figure 4.14 shows the modeled average fume deposit growth rates on the different super-

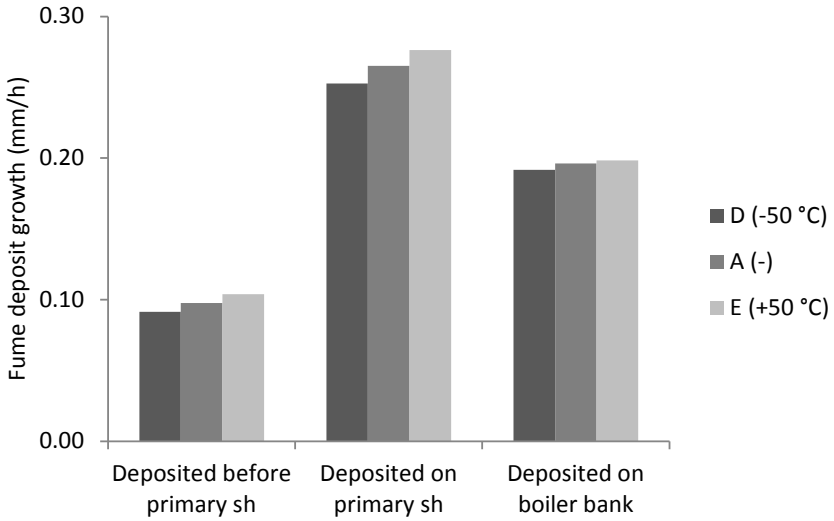

Fig. 4.14: Modeled average instantaneous fume deposit growth rates (mm/h) on the different superheater surfaces when the flue gas inlet temperature is changed. The results are presented for a constant flue gas flow rate (Paper IV).

heater surfaces when the flue gas temperature is changed. The deposit chlorine content is not presented here because the chlorine content is probably highly dependent on the release factors, and thus the effect of the changing flue gas temperature on chlorine content cannot be investigated.

The fume deposit growth rate on all surfaces seems to increase when the flue gas temperature increases. This can again be explained by the increasing temperature gradients between the flue gas and the deposit surfaces. In reality, the increase in the growth rate could be even higher because now the elemental release factors are kept constant. It is known that increasing the furnace temperature increases the amount of the circulating dust and thus deposition [31, 101], but these results indicate that the rate of fume deposition can increase even though the total amount of circulating dust would not increase.

Chapter 5

Summary and conclusions

The kraft recovery boiler has an important role in the pulp-making process because it recovers the cooking chemicals used in the process and produces energy. Earlier, this energy was considered a by-product, but modern recovery boilers are now able to produce as much as 200 MW of electricity [102]. However, further increase in electricity production is often hindered by the ash-forming elements in black liquor, which force the steam temperatures to be limited to relatively low values to avoid corrosion. When the ash-forming elements form fine particles that deposit on the heat transfer surfaces, fouling of the heat transfer surfaces and plugging of the flue gas channels can occur. Understanding the behavior of the ash-forming elements and the formation of fume particles and deposits can help to avoid these problems, but it is difficult to capture the fine particle dynamics with experimental methods alone.

The objective of this thesis work was to develop a computational model for the condensed alkali metal (Na and K) compounds, and to use the model to gain new information on the alkali metal behavior. The model combines CFD (computational fluid dynamics), equilibrium chemistry, and fine particle dynamics. This distinguishes it from the earlier models of Jokiniemi et al. [2], which used only equilibrium chemistry with fine particles dynamics, and of Verrill and Wessel [7] and Wessel et al. [8, 30, 45], which used equilibrium chemistry with CFD. The model focuses on the condensed fine particles in the recovery boiler, called fume, which are below 1 μm in diameter. The small size and the formation mechanism distinguish fume particles from carryover particles, which have been investigated elsewhere [39, 40], and are not a focus of this work. In fact, fume deposition may be more significant than carryover deposition in the superheater area of the boiler because there the fume particles are so numerous that the total mass of the fume particles is usually higher than the total mass of the carryover particles [9].

The model developed here has been applied to two recovery boiler cases (Boilers A and B), which allowed for the partial validation of the model in the superheater area of the boiler. The model is not capable of predicting the conditions in the lower furnace accurately due to the partly reducing atmosphere there, though this is not considered a significant drawback since the majority of fume forms in

the upper furnace and in the superheater area. However, the model has not been completely validated in the superheater area either, because the gas-particle equilibrium for the alkali chlorides could not be accurately measured. Nevertheless, apart from chlorine, the simulated fume particle composition corresponds closely to the measurement results in Boiler B. For fume deposit formation, the modeling results show how deposition by thermophoresis is predominant, and this finding has been made by other researchers as well [2, 78]. Furthermore, in the modeled boiler, the thermophoretic velocity seems to be highest on the primary superheater, and this observation is also supported by the experience of the boiler plugging at that location.

In addition to comparing the modeling results with measurements, model sensitivity analysis has been conducted with respect to a changing deposit thickness on the primary superheater and a changing flue gas temperature. There were two reasons for the sensitivity analysis: to investigate how dependent the model is on the given boundary conditions, and to simulate the effect of some operational changes in real recovery boilers. The results of the sensitivity analysis show that fume deposit growth seems to be a self-limiting process, because when the deposit thickness on one superheater grows, the thermophoretic velocity on that superheater decreases due to a decreasing temperature gradient and an increasing average flue gas temperature. On the other hand, a thick deposit on one superheater may increase deposition on the other heat transfer surfaces downstream. This phenomenon, which is caused by the increasing flue gas temperature, has earlier been demonstrated only for carryover particles [33]. Furthermore, the fume deposition seems to increase when the flue gas temperature entering the superheater area is increased, even if the release factors of the elements are held constant. This is a novel result because, earlier, the increasing fume deposition in this situation has been explained only by the increased volatilization of sodium, potassium, and chlorine [101].

The chlorine content of the deposits was investigated in more detail. The chlorine fraction of the deposits seems to be highest in the deposit layers that form closest to the tube surfaces. This occurs mainly because the rate of deposition by thermophoresis is higher when the deposit surface temperature is lower, and at lower temperatures the fume particles contain more chlorine. However, the lower surface temperature also makes the alkali chlorides more supersaturated near the surface, which makes some alkali chlorides condense directly on the surface, and not on the particles first. This means that the deposit chlorine content may indeed vary between the different superheater areas and even between the different layers of a deposit, although sintering, which was not modeled in this work, may remove the composition differences between the layers. Furthermore, a recent publication [100] has shown that another explanation for the higher chlorine content near the tube surfaces may be the migration of the alkali chloride vapors inside the deposit.

Several approximations have been made in the presented model to make its use feasible and relatively efficient. The main approximation is the steady-state assumption, which means that the modeling results are valid only for one instant in time and for the given boundary conditions. Because of this limitation, the model's sensitivity to the deposit thickness boundary condition was investigated

in Chapter 4.4. Another limitation is that the presented modeling results are not perfectly grid-independent, but here again a compromise has been made between modeling accuracy and time consumption. Furthermore, although the equation for thermophoresis was shown to be adequate in the simulated conditions, it is only approximate at low temperatures and for particles approaching a diameter of 1 µm. Nevertheless, the equation has the advantage of not being dependent on the particle size distribution, which is not reliably known. The ideal solution assumption on the surface of condensed particles could also be considered an over-simplification. Moreover, the constant elemental release factors used introduces uncertainty to the modeling results.

To summarize, the main contributions of this thesis are:

- Improving the understanding of alkali metal chemistry, fume particle formation and fume deposit growth in recovery boilers.
- Developing a 3-dimensional CFD-based model, which utilizes equilibrium chemistry and fine particle dynamics, and which can be used as a tool in recovery boiler design.
- Facilitating the prediction of fouling and plugging of the heat transfer surfaces together with the consequential corrosion conditions.
- Suggesting that fume deposition in the recovery boiler is dominated by thermophoresis.
- Suggesting that the local chlorine content of the fume deposits is highly temperature-dependent.

Chapter 6

Future work

In terms of future plans, the most important development is to complete the validation of the model by conducting measurements in a boiler burning black liquor with high Cl and K contents, and also by modeling the same boiler. It would be important to capture the gas-particle equilibrium of the alkali chlorides in the new measurements, but this is challenging. One possibility is to use laser measurements to determine the gaseous KCl concentration in the boiler [103], but this method has not yet been tested in recovery boilers. There is also a need to obtain measurement results for deposit composition and growth rate at different locations in the boiler. Measurements of deposit chlorine content as a function of distance from the superheater tubes would also be needed to validate the results of the sensitivity analysis. Moreover, the model sensitivity analysis should be extended to include the black liquor composition and the elemental release factors.

The actual fume particle dynamics and deposition model could be developed further. For example, time-dependent modeling could be attempted, which would allow the simulation of changing deposit growth rate. The presented model contains several submodels, some of which are oversimplified and would need to be modified in the future. One such submodel assumes constant release factors for the ash-forming elements from black liquor. Here the work of Jukola et al. [54] could be utilized to model the release of sodium more accurately. Another example is the assumption of ideal solutions on the surface of the fume particles, which could be improved by modeling the non-ideal interactions of the salt ions. Furthermore, the Talbot equation for thermophoresis [80] could replace the simpler equation now used if more reliable information on the particle size distribution was available. Validation of the submodels in smaller scale experiments would also support the results obtained by the model.

Because the model contains several simplifications and has not been fully validated, the model developed here is not yet claimed to provide quantitative results. Instead, the model is considered a useful tool for investigating the effect of changing operation parameters on the behavior of alkali metal compounds. The model is not a stand-alone model and needs to be combined with existing recovery boiler geometries and models for black liquor combustion. Combining

the model with other models for the release of ash-forming elements or for carryover particles could make it more comprehensive. However, the model already provides new information on fume particles and deposits, and it can be used in recovery boiler design to help to minimize fouling, plugging, and corrosion problems. In the future, the modeling principle could also be applied to other biomass-fired boilers, such as the bubbling fluidized bed boilers, although the different chemical compounds and the particles in the bed material should then be taken into account.

Bibliography

[1] Jokiniemi, J. K., Lazaridis, M., Lehtinen, K. E. J., and Kauppinen, E. I. Numerical simulation of vapour-aerosol dynamics in combustion processes. *Journal of Aerosol Science*, 25(3):429–446, 1994.

[2] Jokiniemi, J. K., Pyykönen, J., Mikkanen, P., and Kauppinen, E. I. Modeling fume formation and deposition in kraft recovery boilers. *TAPPI Journal*, 79(7):171–181, 1996.

[3] ANSYS Inc. *ANSYS Academic Research, Release 14.5*, 2013.

[4] Particle Dynamics GmbH. *Fine Particle Model (FPM) for FLUENT. User's Guide*, 2003.

[5] Arakawa, Y., Ukeguchi, Y., Maeda, T., Sakai, T., and Tran, H. Maximizing the electricity generation capacity of recovery boilers and superheater tube materials in Japanese pulp and paper mills. In *Proceedings of the International Chemical Recovery Conference, vol. 1*, p. 37–49, Tampere, Finland, 2014.

[6] Hupa, M. Recovery boiler research highlights - 10 steps forward. In *Continuous development of recovery boiler technology - 50 years of cooperation in Finland*, p. 7–18, Tampere, Finland, 2014.

[7] Verrill, C. L. and Wessel, R. A. Detailed black liquor drop combustion model for predicting fume in kraft recovery boilers. *TAPPI Journal*, 81(9):139–148, 1998.

[8] Wessel, R. A. and Baxter, L. L. Comprehensive model of alkali-salt deposition in recovery boilers. *TAPPI Journal*, 2(2):19–24, 2003.

[9] Mikkanen, P. *Fly Ash Particle Formation in Kraft Recovery Boilers*. Doctoral dissertation, 2000.

[10] Grace, T. M. A critical review of computer modeling of kraft recovery boilers. *TAPPI Journal*, 79(7):182–190, 1996.

[11] Hupa, M., Engblom, M., Brink, A., and Mueller, C. How well do we understand recovery furnace processes? In *45 years recovery boiler cooperation in Finland*, p. 17–29. Finnish Recovery Boiler Committee, 2009.

[12] Tomlinson, G. H. and Wilcoxson, L. S. Method of and apparatus for burning waste liquor, 1935.

[13] Vakkilainen, E., Kuparinen, K., and Heinimö, J. Large industrial users of energy biomass. Technical report, IEA Bioenergy, 2013.

[14] Tilastokeskus. Suomen virallinen tilasto (SVT). Energian hankinta ja kulutus (Electronic publication), 2013.

[15] Kara, M., Mattila, L., Viinikainen, S., Wolff, J., and Lind, I. *Energia Suomessa*. 2004.

[16] European Commission. Directive 2009/28/EC. *Official Journal of the European Union Belgium*, 2009.

[17] Valmet. One of the world's largest pulp mills supplied by Valmet successfully started up in Brazil. `http://www.valmet.com/en/infocenter/news.nsf/NewsItems/1753021`. Accessed: 05/2014.

[18] Maakala, V. and Miikkulainen, P. Dimensioning a recovery boiler furnace using mathematical optimization. In *Proceedings of the International Chemical Recovery Conference, vol. 2*, p. 75–88, Tampere, Finland, 2014.

[19] Adams, T. *Kraft Recovery Boilers*. TAPPI Press, Atlanta, 1997.

[20] Vakkilainen, E. *Kraft Recovery Boilers - Principles and Practice*. Valopaino Oy, Helsinki, 2005.

[21] Hocking, M. *Handbook of Chemical Technology and Pollution Control*. Academic Press, Oxford, 3rd edition, 2005.

[22] Tandra, D., Miikkulainen, P., and Savolainen, J. Energy saving & cost reduction through the use of 9-14 bar steam from turbine extraction for sootblowing: a case study. In *Proceedings of the International Chemical Recovery Conference, vol. 1*, p. 129–135, Tampere, Finland, 2014.

[23] Skrifvars, B.-J., Backman, R., Hupa, M., Salmenoja, K., and Vakkilainen, E. Corrosion of superheater steel materials under alkali salt deposits. Part 1: The effect of salt deposit composition and temperature. *Corrosion Science*, 50:1274–1282, 2008.

[24] Tamminen, T., Kiuru, J., Kiuru, R., Janka, K., and Hupa, M. Dust and flue gas chemistry during rapid changes in the operation of black liquor recovery boilers: Part 1 - dust formation. *TAPPI Journal*, 1(5):27–32, 2002.

[25] Borg, A., Teder, A., and Warnqvist, B. Inside a kraft recovery furnace - studies on the origins of sulfur and sodium emission. *Tappi*, 57(1):126–129, 1974.

[26] Wåg, K. J., Reis, V. V., Frederick, W. J., and Grace, T. M. Mathematical model for the release of inorganic emissions during black liquor char combustion. *TAPPI Journal*, 80(5):135–145, 1997.

[27] Sippula, O., Lind, T., and Jokiniemi, J. Effects of chlorine and sulphur on particle formation in wood combustion performed in a laboratory scale reactor. *Fuel*, 87(12):2425–2436, 2008.

[28] Pyykönen, J. and Jokiniemi, J. Modelling alkali chloride superheater deposition, and its implications. *Fuel Processing Technology*, 80(3):225–262, 2003.

[29] Lien, S. and Verrill, C. Particulate emissions from char bed burning. In *1998 International Chemical Recovery Conference, vol. 2*, p. 1023–1040, Tampa, FL, 1998.

[30] Wessel, R. A., Baxter, L. L., Shaddix, C., Verrill, C. L., Frederick, J., Lien, S. J., and Tran, H. Particle formation and deposition in kraft recovery boilers. In *2004 International Chemical Recovery Conference*, volume 1, p. 363–379, Charleston, SC, 2004.

[31] Mikkanen, P., Kauppinen, E. I., Pyykönen, J., Jokiniemi, J. K., Aurela, M., Vakkilainen, E. K., and Janka, K. Alkali salt ash formation in four Finnish industrial recovery boilers. *Energy & Fuels*, 13(4):778–795, 1999.

[32] Eskola, A., Jokiniemi, J., Lehtinen, K., and Vakkilainen, E. Modelling alkali salt deposition on kraft recovery boiler heat exchangers in the superheater section. In *Proceedings of the 1998 International Chemical Recovery Conference*, p. 469–486, Tampa, FL, 1998.

[33] Tran, H. *Upper Furnace Deposition and Plugging*, p. 245–282. Kraft Recovery Boilers. TAPPI Press, Atlanta, 1997.

[34] Hinds, W. *Aerosol Technology. Properties, Behavior, and Measurement of Airborne Particles*. John-Wiley & Sons, Inc., New York, 2nd edition, 1999.

[35] Grace, T., Walsh, A., Jones, A., Sumnicht, D., and Farrington, T. A three-dimensional mathematical model of the kraft recovery furnace. In *1989 International Chemical Recovery Conference Proceedings*, Montreal, Canada, 1989.

[36] Karvinen, R., Hyöty, P., and Siiskonen, P. The effect of dry solids content on recovery boiler furnace behavior. *TAPPI Journal*, 74(12):171–177, 1991.

[37] Ferreira, D. J. O., Cardoso, M., and Park, S. W. Gas flow analysis in a kraft recovery boiler. *Fuel Processing Technology*, 91(7):789–798, 2010.

[38] Engblom, M. *Modeling and field observations of char bed processes in black liquor recovery boilers*. Doctoral dissertation, 2010.

[39] Wessel, R. A., Parker, K. L., and Verrill, C. L. Three-dimensional kraft recovery furnace model: implementation and results of improved black-liquor combustion models. *TAPPI Journal*, 80(10):207–220, 1997.

[40] Li, B., Brink, A., and Hupa, M. CFD investigation of slagging on a superheater tube in a kraft recovery boiler. *Fuel Processing Technology*, 105:149–153, 2013.

[41] Mueller, C., Selenius, M., Theis, M., Skrifvars, B.-J., Backman, R., Hupa, M., and Tran, H. Deposition behaviour of molten alkali-rich fly ashes - development of a submodel for CFD applications. *Proceedings of the Combustion Institute*, 30(2):2991–2998, 2005.

[42] Strandström, K., Mueller, C., and Hupa, M. Development of an ash particle deposition model considering build-up and removal mechanisms. *Fuel Processing Technology*, 88(11):1053–1060, 2007.

[43] Weber, R., Mancini, M., Schaffel-Mancini, N., and Kupka, T. On predicting the ash behaviour using Computational Fluid Dynamics. *Fuel Processing Technology*, 105:113–128, 2013.

[44] Jöller, M., Brunner, T., and Obernberger, I. Modeling of aerosol formation during biomass combustion for various furnace and boiler types. *Fuel Processing Technology*, 88(11):1136–1147, 2007.

[45] Wessel, R. A., Verrill, C. L., Blue, J. D., and Hiner, L. A. Black liquor combustion model for predicting ash chemistry in kraft recovery boilers. In *AIChE 1998 Annual Meeting*, Miami Beach, FL, 1998.

[46] Eaton, A. M., Smoot, L. D., Hill, S. C., and Eatough, C. N. Components, formulations, solutions, evaluation, and application of comprehensive combustion models. *Progress in Energy and Combustion Science*, 25(4):387–436, 1999.

[47] Ferziger, J. H. and Peric, M. *Computational Methods for Fluid Dynamics*. Springer-Verlag, Berlin Heidelberg, 1997.

[48] Järvinen, M., Zevenhoven, R., Vakkilainen, E., and Forssén, M. Black liquor devolatilization and swelling - a detailed droplet model and experimental validation. *Biomass and Bioenergy*, 24(6):495–509, 2003.

[49] Heikkilä, V.-P. Recovery boiler model, 2010. (Unpublished material).

[50] Tamminen, T., Laurén, T., Janka, K., and Hupa, M. Dust and flue gas chemistry during rapid changes in the operation of black liquor recovery boilers: Part 2 - dust composition. *TAPPI Journal*, 1(6):25–29, 2002.

[51] Mikkanen, P., Jokiniemi, J., Kauppinen, E., and Vakkilainen, E. Experimental and modelling study on the fume formation at a kraft recovery boiler. *Fundamental Advances and Innovations in the Pulp and Paper Industry*, 95(322):103–118, 1998.

[52] Mikkanen, P., Jokiniemi, J., Kauppinen, E., and Vakkilainen, E. Coarse ash particle characteristics in a pulp and paper industry chemical recovery boiler. *Fuel*, 80(7):987–999, 2001.

[53] Kangas, P., Koukkari, P., Lindberg, D., and Hupa, M. Modelling black liquor combustion with the constrained Gibbs energy method. *J-FOR: Journal of Science & Technology for Forest Products and Processes*, 3(3):6–15, 2013.

[54] Jukola, P., Kyttälä, J., and McKeough, P. Predicting sodium release in recovery boilers in conjuction with CFD furnace modelling. In *Proceedings of the International Chemical Recovery Conference, vol. 2*, p. 48–58, Tampere, Finland, 2014.

[55] Saw, W. L., Hupa, M., Ashman, P. J., Nathan, G. J., Forssén, M., and Alwahabi, Z. T. Insight into the fate of atomic sodium from black liquor combustion in a flat flame using equilibrium calculations. In *Proceedings of the Australian Combustion Symposium*, p. 118–121, 2007.

[56] Thermfact & GTT Technologies. Factsage (The Equilib Module - Regular Features), 2009.

[57] Bale, C. W., Bélisle, E., Chartrand, P., Decterov, S. A., Eriksson, G., Hack, K., Jung, I. H., Kang, Y. B., Melancon, J., Pelton, A. D., Robelin, C., and Petersen, S. Factsage thermochemical software and databases - recent developments. *Calphad*, 33(2):295–311, 2009.

[58] Lindberg, D., Backman, R., and Chartrand, P. Thermodynamic evaluation and optimization of the (NaCl Na_2SO_4 Na_2CO_3 KCl K_2SO_4 K_2CO_3) system. *Journal of chemical thermodynamics*, 39(7):1001–1021, 2007.

[59] Lindberg, D., Backman, R., Chartrand, P., and Hupa, M. Towards a comprehensive thermodynamic database for ash-forming elements in biomass and waste combustion - current situation and future developments. *Fuel Processing Technology*, 105:129–141, 2013.

[60] Christensen, K. A. and Livbjerg, H. A field study of submicron particles from the combustion of straw. *Aerosol Science and Technology*, 25(2):185–199, 1996.

[61] Christensen, K. A., Stenholm, M., and Livbjerg, H. The formation of submicron aerosol particles, HCl and SO_2 in straw-fired boilers. *Journal of Aerosol Science*, 29:421–444, 1998.

[62] Uhrner, U., von Löwis, S., Vehkamäki, H., Wehner, B., Bräsel, S., Hermann, M., Stratmann, F., Kulmala, M., and Wiedensohler, A. Dilution and aerosol dynamics within a diesel car exhaust plume-CFD simulations of on-road measurement conditions. *Atmospheric Environment*, 41(35):7440–7461, 2007.

[63] Herrmann, E., Lihavainen, H., Hyvärinen, A. P., Riipinen, I., Wilck, M., Stratmann, F., and Kulmala, M. Nucleation simulations using the fluid dynamics software FLUENT with the fine particle model FPM. *Journal of Physical Chemistry A*, 110(45):12448–12455, 2006.

[64] Herrmann, E., Hyvärinen, A. P., Brus, D., Lihavainen, H., and Kulmala, M. Re-evaluation of the pressure effect for nucleation in laminar flow diffusion chamber experiments with Fluent and the Fine Particle Model. *Journal of Physical Chemistry A*, 113(8):1434–1439, 2009.

[65] Herrmann, E., Brus, D., Hyvärinen, A. P., Stratmann, F., Wilck, M., Lihavainen, H., and Kulmala, M. A computational fluid dynamics approach to nucleation in the water-sulfuric acid system. *Journal of Physical Chemistry A*, 114(31):8033–8042, 2010.

[66] Han, J., Xu, M., Yao, H., Furuuchi, M., Sakano, T., and Kim, H. J. Simulating the transformation of heavy metals during coal or sewage sludge combustion. *Journal of Environmental Science and Health Part A*, 42(2):217–224, 2007.

[67] Whitby, E. and McMurry, P. Modal aerosol dynamics modeling. *Aerosol Science and Technology*, 27:673–688, 1997.

[68] Wilck, M. and Stratmann, F. A 2-D multicomponent modal aerosol model and its application to laminar flow reactors. *Journal of Aerosol Science*, 28(6):959–972, 1997.

[69] Friedlander, S. *Smoke, Dust, and Haze. Fundamentals of Aerosol Dynamics.* Oxford University Press, New York, 2nd edition, 2000.

[70] Pyykönen, J. *Computational Simulation of Aerosol Behaviour.* Doctoral dissertation, 2002.

[71] *DIPPR Project 801 - Full Version.* Design Institute for Physical Property Research/AIChE, 2010. (Electronic publication).

[72] Knacke, O., Kubaschewski, O., and Hesselmann, K. *Thermochemical Properties of Inorganic Substances.* Springer-Verlag, Berlin, 1991.

[73] Frenkel, J. *Kinetic Theory of Liquids.* Dover, New York, 1955.

[74] Sippula, O. *Fine Particle Formation and Emissions in Biomass Combustion.* Doctoral dissertation, 2010.

[75] Barrett, J. and Clement, C. Growth rates for liquid drops. *Journal of Aerosol Science*, 19(2):223–242, 1988.

[76] Dahneke, B. *Simple Kinetic Theory of Brownian Diffusion in Vapors and Aerosols*, p. 97–133. Theory of Dispersed Multiphase Flow. Academic Press, New York, 1983.

[77] Tran, H. How does a kraft recovery boiler become plugged. *TAPPI Journal*, 69(11):102–106, 1986.

[78] Cameron, J. H. and Goerg-Wood, K. Role of thermophoresis in the deposition of fume particles resulting from the combustion of high inorganic containing fuels with reference to kraft black liquor. *Fuel Processing Technology*, 60(1):49–68, 1999.

[79] Sinquefield, S. A., Baxter, L. L., and Frederick, W. J. An experimental study of the mechanisms of fine particle deposition in kraft recovery boilers. In *1998 TAPPI International Chemical Recovery Conference*, p. 443–467, Tampa, FL, 1998.

[80] Talbot, L., Cheng, R. K., Schefer, R. W., and Willis, D. R. Thermophoresis of particles in a heated boundary layer. *Journal of Fluid Mechanics*, 101(4):737–758, 1980.

[81] Davies, C. Definitive equations for the fluid resistance of spheres. *Proceedings of the Physical Society*, 57(4):259–270, 1945.

[82] Lockwood, F. C. and Yousif, S. A model for the particulate matter enrichment with toxic metals in solid fuel flames. *Fuel Processing Technology*, 65:439–457, 2000.

[83] Kær, S. K., Rosendahl, L. A., and Baxter, L. L. Towards a CFD-based mechanistic deposit formation model for straw-fired boilers. *Fuel*, 85(5–6):833–848, 2006.

[84] Waldmann, L. and Schmitt, K. H. *Thermophoresis and diffusiophoresis of aerosols*, p. 137–162. Aerosol Science. Academic Press, London, 1966.

[85] Wells, A. C. and Chamberlain, A. C. Transport of small particles to vertical surfaces. *British Journal of Applied Physics*, 18(12):1793–1799, 1967.

[86] Jokiniemi, J., Pyykönen, J., Lyyränen, J., Mikkanen, P., and Kauppinen, E. *Modelling ash deposition during the combustion of low grade fuels*, p. 591–615. Applications of Advanced Technology to Ash-Related Problems in Boilers. Plenum Press, New York, 1996.

[87] Zbogar, A., Frandsen, F. J., Jensen, P. A., and Glarborg, P. Heat transfer in ash deposits: A modelling tool-box. *Progress in Energy and Combustion Science*, 31(5):371–421, 2005.

[88] Duhamel, M., Tran, H., and Jr., W. J. F. The sintering tendency of recovery boiler precipitator dust. *TAPPI Journal*, 3(10):25–30, 2004.

[89] Frederick, W. J., Vakkilainen, E. K., Tran, H. N., and Lien, S. J. The conditions for boiler bank plugging by submicrometer sodium salt (fume) particles in kraft recovery boilers. *Energy & Fuels*, 18(3):795–803, 2004.

[90] Saario, A. and Oksanen, A. Effect of computational grid in industrial-scale boiler modeling. *International Journal of Numerical Methods for Heat and Fluid Flow*, 19(1):93–117, 2009.

[91] Aho, M., Paakkinen, K., and Taipale, R. Quality of deposits during grate combustion of corn stover and wood chip blends. *Fuel*, 104:476–487, 2013.

[92] Deuerling, C. F., Maguhn, J., Nordsieck, H. O., Warnecke, R., and Zimmermann, R. Measurement system for characterization of gas and particle phase of high temperature combustion aerosols. *Aerosol Science and Technology*, 44(1):1–9, 2010.

[93] Tavares, A. and Tran, H. Field studies on fume chemistry and deposition in kraft recovery boilers. *TAPPI Journal*, 80(12):117–122, 1997.

[94] Kawaji, M., Shen, X. H., Tran, H., Esaki, S., and Dees, C. Prediction of heat transfer in the kraft recovery boiler superheater region. *Tappi Journal*, 78(10):214–221, 1995.

[95] Salmenoja, K. Kraft recovery boiler dust chemistry - implications from operating boilers. In *Proceedings of the International Chemical Recovery Conference, vol. 1*, p. 7–13, Tampere, Finland, 2014.

[96] Tavares, A., Tran, H., Barham, D., Rouilard, P., and Adams, B. Fume chemistry, morphology and deposition in a kraft recovery boiler: fume deposits content and makeup varied across boiler sections. *Pulp and Paper Canada*, 97(10):51–56, 1996.

[97] *Knovel Critical Tables*. Knovel, 2nd edition, 2008. (Electronic publication).

[98] Baxter, L., Hatch, G., Sinquefield, S. A., and Frederick, W. J. An experimental study of the mechanisms of fine particle deposition in kraft recovery boilers. In *2004 International Chemical Recovery Conference*, p. 393–412, Charleston, SC, 2004. TAPPI.

[99] Zhou, H., Jensen, P. A., and Frandsen, F. J. Dynamic mechanistic model of superheater deposit growth and shedding in a biomass fired grate boiler. *Fuel*, 86(10):1519–1533, 2007.

[100] Lindberg, D., Engblom, M., Yrjas, P., Laurén, T., Lindholm, J., and Hupa, M. Influence of deposit aging on superheater corrosion. In *Proceedings of the 2014 International Chemical Recovery Conference, vol. 2*, p. 101–113, Tampere, Finland.

[101] Hupa, M. *Recovery Boiler Chemistry*, p. 39–57. Kraft Recovery Boilers. TAPPI Press, Atlanta, 1997.

[102] Vakkilainen, E. Recovery boilers - history and future. In *Continuous development of recovery boiler technology - 50 years of cooperation in Finland*, p. 19–32, Tampere, Finland, 2014.

[103] Sorvajärvi, T., Saarela, J., and Toivonen, J. Optical detection of potassium chloride vapor using collinear photofragmentation and atomic absorption spectroscopy. *Optics Letters*, 37(19):4011–4013, 2012.

Tampereen teknillinen yliopisto
PL 527
33101 Tampere

Tampere University of Technology
P.O.B. 527
FI-33101 Tampere, Finland

ISBN 978-952-15-3433-1
ISSN 1459-2045